Summer 8-17-2012

High Resolution Observations of 36 GHz Class I Methanol Masers at Sites of 6.7 GHz Class II Methanol Masers in Star Forming Regions

Jared Hennen
DePaul University, JHENNEN88@GMAIL.COM

Recommended Citation

Hennen, Jared, "High Resolution Observations of 36 GHz Class I Methanol Masers at Sites of 6.7 GHz Class II Methanol Masers in Star Forming Regions" (2012). *College of Science and Health Theses and Dissertations*. 19.
https://via.library.depaul.edu/csh_etd/19

DEPAUL UNIVERSITY

High Resolution Observations of 36 GHz Class I Methanol Masers at Sites of 6.7 GHz Class II Methanol Masers in Star Forming Regions

by

Jared Hennen

A thesis submitted in partial fulfillment for the
degree of Master of Science

in the
Department of Physics
College of Science and Health

August 2012

Contents

List of Figures

List of Tables

Abbreviations

AIPS	**A**stronomical **I**mage **P**rocessing **S**ystem
Dec.	**Dec**lination
FWHM	**F**ull **W**idth at **H**alf **M**aximum
LSR	**L**ocal **S**tandard of **R**est
MASER	**M**icrowave **A**mplification by **S**timulated **E**mission of **R**adiation
NRAO	**N**ational **R**adio **A**stronomy **O**bservatory
PA	**P**osition **A**ngle
R.A.	**R**ight **A**scension
VLA	Karl G. Jansky **V**ery **L**arge **A**rray

Acknowledgements

I would like to express my sincere gratitude to my advisor, Dr. Anuj Sarma, who has guided me through this process with much patience. This thesis would not have been possible without his supervision and encouragement; the knowledge he has shared with me is invaluable. I also want to thank the members of my defense committee, Dr. Jesús Pando and Dr. Gabriela González Avilés, for committing their time to review my thesis. I would like to thank both Wale Afolayan and Josh Modica for the work they did in performing the Gaussian fits on each velocity profile. My family and friends, and in particular Jennifer Smith, have done a lot to help me through this process and for that I thank them. Finally, I would like to thank the faculty in the Physics Department at DePaul University for all the years they have spent with me and for all I have gained from my time with them.

DEPAUL UNIVERSITY

Abstract

Department of Physics
College of Science and Health

Master of Science

by Jared Hennen

In this thesis we present high angular resolution data on 36 GHz Class I methanol masers associated with sites of 6.7 GHz Class II methanol masers. We observed twenty-three 36 GHz Class I methanol masers in seven star forming regions with the Jansky Very Large Array radio telescope. Our observations have made possible the first high angular resolution maps of 36 GHz masers in several star forming regions, and demonstrated cases where the morphology is highly suggestive of arcs and other structures known to be found at shock interfaces in such regions. The two classes of methanol masers are created through different excitation processes, and occur in different parts of star forming regions. We find that strong 6.7 GHz Class II maser sites are likely associated with weak 36 GHz Class I masers, in agreement with a similar anti-correlation between 44 GHz Class I and 6.7 GHz Class II methanol masers in the literature. However, there is a correlation between 95 GHz Class I and 6.7 GHz Class II masers in the literature. This points to the need for a larger set of high angular resolution data and improved theoretical models of methanol maser pumping and propagation. We find that the center velocities (v_{LSR}) of the observed 36 GHz masers are quite close to the v_{LSR} of 6.7 GHz masers, and in some cases may be closer to the systemic velocity of the region than the v_{LSR} of the 6.7 GHz masers. This could be due to such 36 GHz masers being located at the base of outflows close to the location of the protostar. Finally, comparison of spectral profiles indicates that the strongest 36 GHz masers may lie closer to the 6.7 GHz masers. In summary, such high angular resolution observations that allow for the comparison of the two classes of methanol masers provide a powerful tool to study star forming regions.

Chapter 1

Introduction

Masers are a valuable tool for studying star forming regions at high angular resolution because they are compact and bright sources. This is especially important when studying high-mass star forming regions at high resolution because they tend to be located much farther than low mass star forming regions. The process of forming these high-mass stars, characterized by masses of 8 times that of our Sun or greater, is not currently fully understood. These high-mass stars are important to understanding not only our Galaxy but others as well. They are constantly feeding matter and energy into the interstellar medium, starting when they are forming (in the form of mass outflows and radiation) until the end of their life cycles (when they create the heavier elements as supernovae). In particular, methanol masers offer a great opportunity to probe these regions because of the large number of methanol maser lines. However, we still have much to learn about methanol masers. In this thesis, we will be looking at some of the earliest available high angular resolution data on 36 GHz Class I methanol masers, taken while 36 GHz receivers were still being installed on the Jansky Very Large Array (VLA), and examine their potential for the study of high-mass star forming regions. Since these masers are located at 6.7 GHz Class II methanol maser sites, and the two maser classes have different pumping conditions, we will investigate how exploring the connections between these two species helps us learn about the star formation process.

In the rest of this chapter we will give an introduction to the process of star formation, explore basic maser theory, the methanol molecule, and the associated transitions for 36 GHz Class I and 6.7 GHz Class II masers. This will all be brought together to provide an overview of the motivation for this pilot survey. Chapter two will include an overview of radio interferometry and data acquisition with the VLA, data calibration, imaging, and the parameters and reduction process for our 36 GHz methanol maser observations. Chapter three presents the results from our 36 GHz methanol maser observations, and in

Chapter four we discuss our results, including a comparison to 6.7 GHz Class II methanol maser data taken from the literature. In Chapter five, we present our conclusions.

1.1 Star Formation

Stars form within molecular clouds in the interstellar medium. When such a cloud collapses due to its own gravity, the gas and dust will heat up. The process continues with material being accreted onto the protostar from a disk around the protostar. This is also accompanied by the ejection of dust and gas along a direction perpendicular to the accretion disk. These features are called bipolar outflows because they typically occur in pairs in opposite directions, an example of what these structures may look like can be seen in Figure 1.1. While this sequence of events is well known for low mass stars, there is some debate about the exact timeline of these events for high-mass stars. The situation is complicated by the fact that high-mass stars begin radiating even as material is collapsing onto the central protostar. Nevertheless, disks and outflows are known to be part of the high-mass star formation process. It is in the shocked regions along outflows and the region around the protostar that different kinds of masers are known to form. We will now discuss how two of these maser types, the 36 GHz Class I and 6.7 GHz Class II methanol masers, are thought to connect to the star formation process after an introduction to general maser theory.

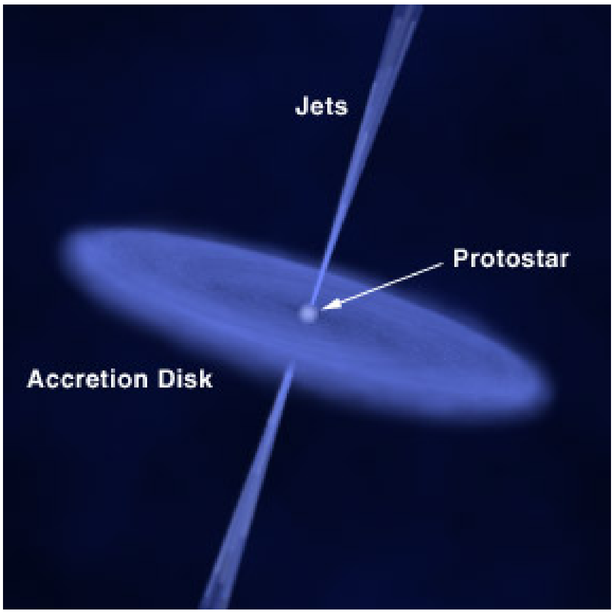

Figure 1.1: Artist's interpretation of a protostar. The accretion disk and bipolar outflows (labeled jets) are both shown. Image courtesy of Hong Kong University.

1.2 Maser Theory

The word *MASER* is an acronym similar to *LASER*, and stands for Microwave Amplification by Stimulated Emission of Radiation. The fundamental theory of this phenomenon is best understood by looking at two-level systems. A two-level maser requires the energy levels within the population to be inverted, which is to say a higher proportion of the molecular population is in the upper energy level. In practice a two-level system is not invertible, but this inversion can take place within the complicated energy levels of molecules. In order for this inversion to occur energy must be pumped into the system somehow, and the upper level should be metastable. This is to say that the stability of the upper level must be high enough so that the rate of excitation is higher than that of the mean decay rate.

Once the energy levels have reached inversion, stimulated emission will lead to a cascade of photons that produces amplification along favored paths. The process of stimulated emission can be seen in the diagram in Figure 1.2. As photons with the same energy corresponding to the energy level difference for the two states pass through the masing region, more photons of the same energy will be emitted. This process leads to intense beams of single frequency light. One major difference between laboratory lasers and astronomical masers is that while naturally occurring masers get amplified as they propagate along a large column, lab lasers require mirrors and other optical equipment in order to mimic this large cavity.

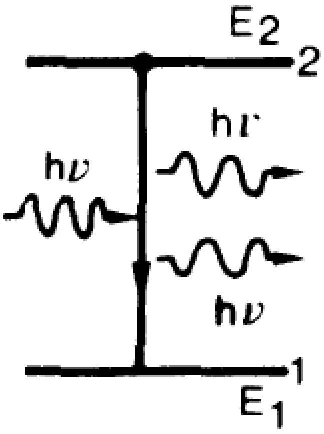

FIGURE 1.2: Diagram showing the process of stimulated emission (Svelto 2009).

Not all paths through a cloud will give amplification, however. If the Doppler shift of the photons is far from that of the molecule it hits, it will not cause stimulated emission because of the shift in frequency. Maser amplification is only achieved along those directions through the cloud that maintain the required velocity coherence. Moreover, the longer the path along which velocity coherence can be maintained, the greater is the amplification. This explains why masers are compact and intense sources. Finally, turbulent motions in clouds lead to significant broadening of non maser lines like CO, OH, etc., but masers are only amplified along paths of velocity coherence. Therefore masers will always have smaller linewidths compared to non maser emission lines from the same region.

1.2.1 Theory for Methanol Masers

Methanol masers were originally divided into two classes based on being far away from known indicators of star formation (Class I) or being close to them (Class II) (Menten 1991). It is now known that the pumping mechanisms, or method of excitation that creates population inversions, of these two classes are different. Class I masers are collisionally pumped while Class II masers are pumped radiatively. Both of these mechanisms come from the process of star formation. Radiative excitation will occur both from thermal emission of dust in early stages of the process, and the emissions of the protostar later on. Collisional excitation may come from various sources, including shockwaves sent out through the cloud as the cloud collapses or outflows discussed in the previous section. Indeed, surveys have confirmed that Class I methanol masers are associated with outflows in star forming regions. This close tie between the conditions necessary for masing to occur and the evolution of star forming regions makes them strong tools for understanding the star forming process.

1.3 Methanol Molecule

The methanol molecule, seen in Figure 1.3, has two different symmetries, called A-type and E-type. These two types of methanol differ by their nuclear spin alignment. In A-methanol the spins of all three hydrogen atoms attached to the carbon atom are parallel, while in E-methanol the spins are not and result in a total nuclear spin of 1/2. All common pumping processes will not convert A-type to E-type or vice versa so they are treated as independent molecules (Cragg et al. 2005). Additionally, these types are often considered to be of equal population, except when formed in low temperature conditions where the A-type has a slightly higher proportion.

This gives us two different energy level diagrams which can be seen in Figures 1.4 and 1.5. The 36 GHz transition occurs in E-type methanol from the $J_k = 4_{-1}$ state to the 3_0 state, where J is the overall angular momentum quantum number and k is J's projection along the major axis of the molecule. This is a common transition for collisionally excited methanol because excitation through collisions tend to favor excitation to states with the same k value. Looking at Figure 1.5 we see that the ground state for the E-type has a k value of -1, hence the preference for excitation to the 4_{-1} state. The 6.7 GHz transition occurs in A-type methanol from the 5_1 state to the 6_0 states.

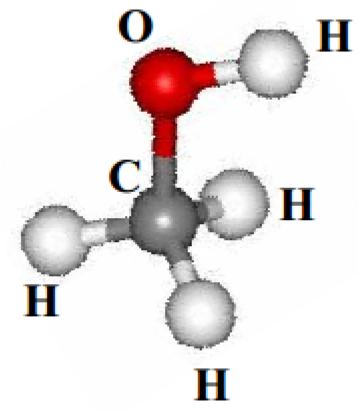

FIGURE 1.3: Diagram of the methanol molecule (Leurini et al. 2004).

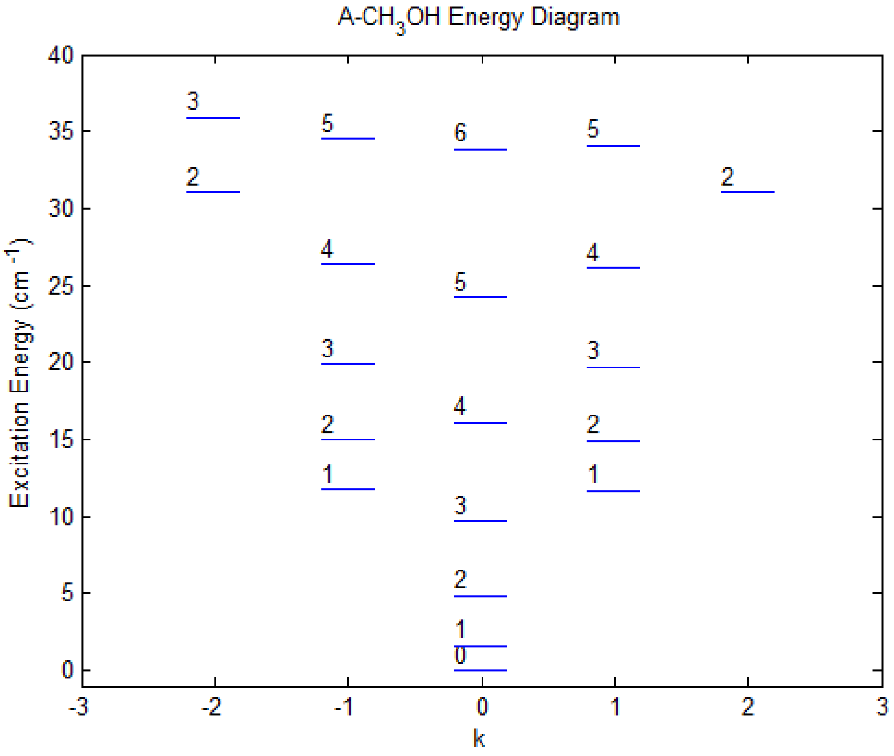

FIGURE 1.4: Energy level diagram of type-A methanol. The vertical axis is energy above the ground state in cm^{-1}, the numbers over each bar show the level's angular momentum quantum number J, and the horizontal axis is the quantum number k. Data to create this figure taken from LAMBDA 2010.

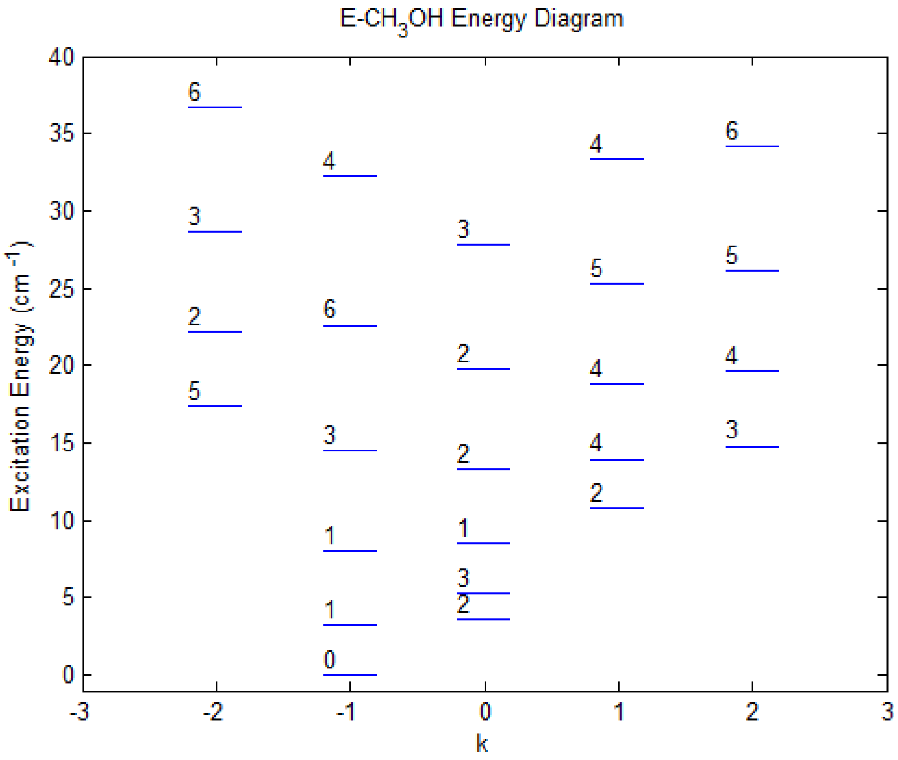

FIGURE 1.5: Energy level diagram of type-E methanol. The vertical axis is energy above the ground state in cm^{-1}, the numbers over each bar show the level's angular momentum quantum number J, and the horizontal axis is the quantum number k. Data to create this figure taken from LAMBDA 2010.

1.4 Motivation

1.4.1 Why Methanol Masers

Methanol masers have been found in many star forming regions, and are unique in their broad range of transition frequencies as well as excitation methods. Class I masers, which include the 36 GHz masers we will focus on, are excited through collisions with shockwaves emanating from the protostar or collapsing core. Class II masers, which include the 6.7 GHz masers we will be comparing to, are excited through radiative processes from the forming protostar and heated dust nearby. Because these two classes of masers are excited in such different ways, both of which rely on the star formation process, they give us a unique opportunity to better understand the star formation process. By examining the possible connection between 36 GHz and 6.7 GHz masers, we hope to further the understanding of how they relate to processes occurring within these regions.

1.4.2 Why These Masers

There have been studies that have compared data of Class I and Class II methanol masers and looked for possible correlation or anti-correlation between these types. There have been arguments for both correlation and anti-correlation, with papers tending to find both intensity and velocity comparisons supporting their case (Slysh et al. 1994; Ellingsen et al. 2004). Recently, there have been arguments made that not all Class I masers will be related to Class II masers in the same way. Indeed, some pumping models predict a correlation between the 36 GHz Class I and 6.7 GHz Class II maser types. However, since no interferometer had a 36 GHz receiver until the time of these observations, no studies exist comparing high angular resolution observations of 36 GHz Class I methanol masers with any Class II methanol masers. By taking advantage of the availability of these 36 GHz receivers even as they were being installed on the VLA, this thesis provides an important pilot study to investigate the potential of this comparative approach.

Chapter 2

Observations and Data Reduction

In this chapter, we discuss the theory of radio interferometry and the calibration and reduction of VLA data. In § 2.1, we give a general overview of radio interferometry. In § 2.2 and § 2.3, we describe the calibration and imaging of interferometry data respectively, and in § 2.4, we discuss the observational parameters of our data and the steps we followed to prepare a data cube and extract useful information from it.

2.1 Radio Interferometry

The 36 GHz methanol maser transition lies within the radio regime. The advantage of this is that these long wavelengths have a much larger mean free path through the gas and dust found within the interstellar medium (ISM), allowing us to observe radiation coming from deep within star forming regions using radio telescopes. The major disadvantage of radio astronomy, however, is that in order to obtain a high angular resolution, the diameter of the antenna has to be very large. The 36 GHz transitions we are observing have wavelengths around the order of a centimeter. If we were to use a single dish to attain an angular resolution on the order of arcseconds comparable to the resolution in the VLA observations reported in this thesis, we would require a dish with a diameter of just over one kilometer. Since such large single dishes would not be practical, we must look for alternatives. Luckily, it turns out that combining signals from multiple antennas gives an angular resolution that is determined by the distance between antennas. Such an instrument is called an interferometer. Below, we discuss the basic idea of the working of an interferometer.

To simplify the analysis, we begin by considering a two-element interferometer, an interferometer made by combining the signals from two antennas, as shown in Figure 2.1. The first antenna receives a voltage signal from a point source given by

$$V_1 = V_o \cos(\omega t) \tag{2.1}$$

where V_o is the amplitude of the signal, ω is the angular frequency of the signal, and t is the time. When the point source is directly above the center of our synthesized antenna, the signal received by the second antenna will be in phase with the first. When this is not the case, there is a time offset so that the voltage signal at the second antenna can be written as

$$V_2 = V_o \cos[\omega(t - \tau)] \tag{2.2}$$

where τ is the time offset given by $\tau = \vec{b} \cdot \hat{s}/c$. Here, $\vec{b}$ is the baseline vector between the two antennas, $\hat{s}$ is the unit vector to the source, and c is the speed of light (Figure 2.1).

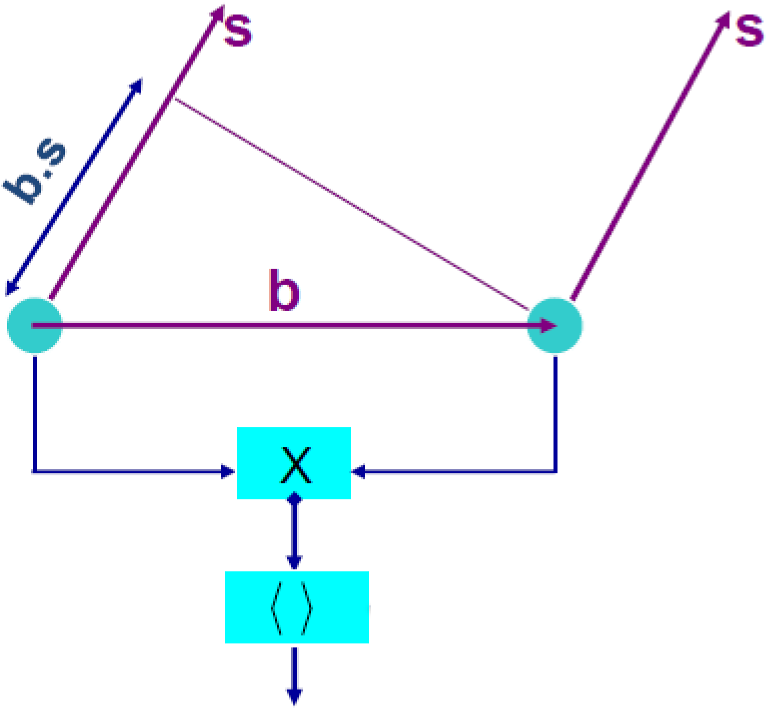

FIGURE 2.1: Diagram showing an interferometer with two antennas. The baseline vector $\vec{b}$ and unit vector to the source $\hat{s}$ are labeled. The × and ⟨⟩ symbol refer to the multiplication and averaging of the signals from the two antennas performed by the correlator. Image taken from Perley 2012.

When these two signals are combined together by multiplying equations (2.1) and (2.2), we can use the trigonometric identity

$$\cos\theta_1 \cos\theta_2 = \frac{\cos(\theta_1 - \theta_2) + \cos(\theta_1 + \theta_2)}{2} \tag{2.3}$$

to express the result as a product of two cosine terms, one of which varies with time ($\cos[2\omega t - \omega\tau]$), and the other does not ($\cos\omega\tau$). Upon averaging therefore, we obtain

$$R_c^* = I\cos(\omega\tau) \tag{2.4}$$

where I is the intensity of the point source, given by $I = V_o^2/2$. In reality, we usually observe sources with spatial extent, so we must integrate over the solid angle. This gives us our final formula for R_c

$$R_c = \iint I\cos(\omega\tau)d\Omega \tag{2.5}$$

R_c is called the *correlator response*, and is the result of multiplying and averaging the signals received at the two antennas. However, equation (2.5) is not enough to recover the full source intensity. For example, if the source being observed has a component with odd symmetry, we will get $R_c = 0$ because the cosine is an even function. Therefore, to recover the full intensity, we also need a sine component. This is done by introducing a $\pi/2$ phase offset in the signal path of one of the antennas and gives us R_s, which is defined the same as R_c except the cosine function in equation (2.5) is replaced by a sine function. The final result is combined in the visibility function

$$V = R_c - iR_s \tag{2.6}$$

By combining equations (2.5) and (2.6) we get

$$V = \iint \Big[I\cos(\omega\tau) - iI\sin(\omega\tau)\Big]d\Omega \tag{2.7}$$

which can be rewritten as

$$V = \iint Ie^{-i\omega\tau}d\Omega \tag{2.8}$$

Expanding τ out, we get

$$V = \iint Ie^{-i\omega\vec{b}\cdot\hat{s}/c}d\Omega \tag{2.9}$$

where V is a function of $\vec{b}$ and I is a function of $\hat{s}$.

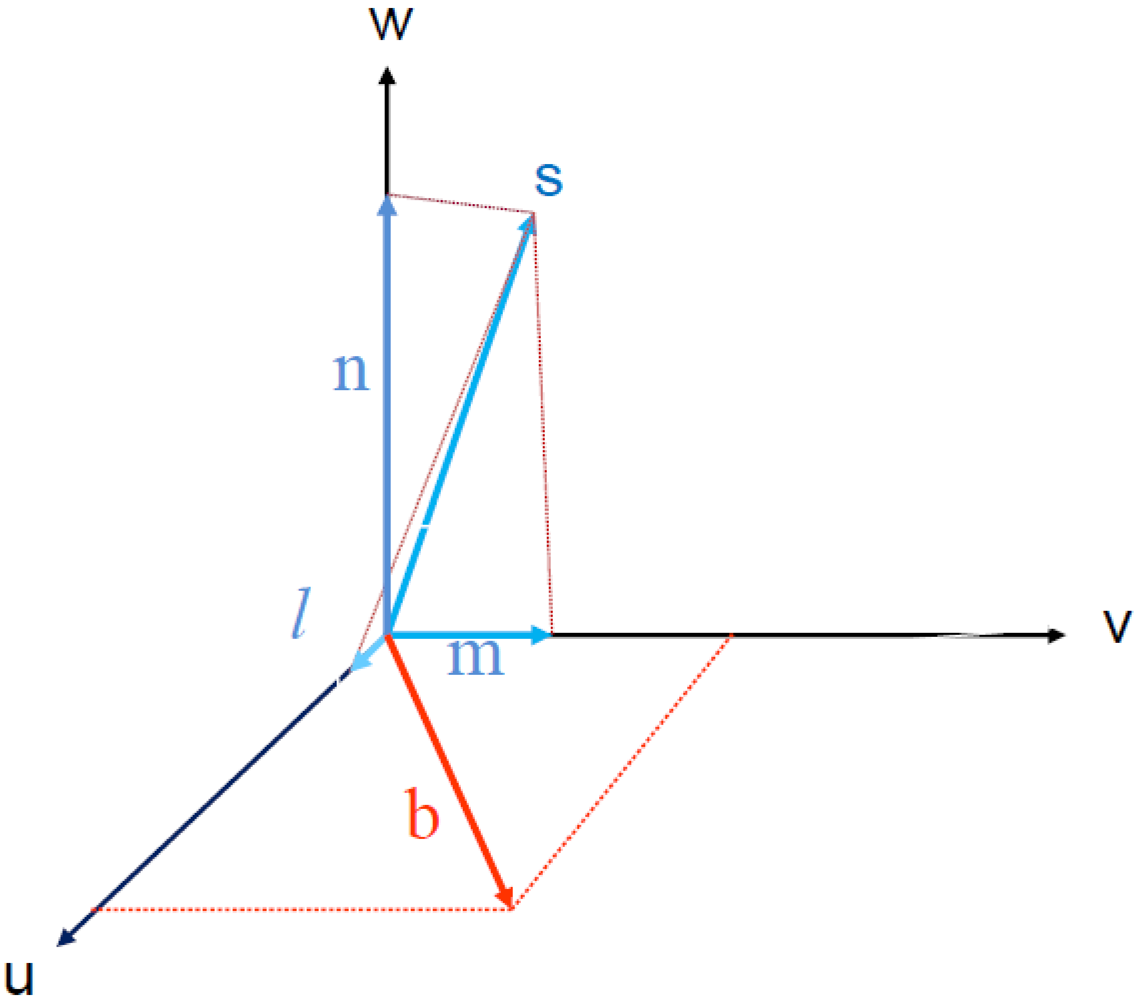

FIGURE 2.2: Diagram showing the (u, v, w) coordinate system. The baseline vector $\vec{b}$ and unit vector $\hat{s}$ toward the source along with its projections (l, m, n) on to the (u, v, w) axes are also shown. Image taken from Perley 2012.

So far, the theory discussed has been for two antennas, but in practice the array consists of more than two antennas. To keep track of these antennas, it is convenient to define a coordinate system (u, v, w), as shown in Figure 2.2. We assume that the visibility function lies on the (u, v) plane and that the w-axis is perpendicular to the (u, v) plane. Our baseline vector can then be defined by

$$\vec{b} = (\lambda u, \lambda v, \lambda w) = (\lambda u, \lambda v, 0) = \lambda u\hat{u} + \lambda v\hat{v} \tag{2.10}$$

where $\hat{u}$ and $\hat{v}$ are unit vectors along the u and v axes respectively, and u and v may be expressed in units of wavelength. Similarly, we have the coordinates (l, m, n) of $\hat{s}$ along the u, v, w axes, giving us

$$\hat{s} = (l, m, n) = l\hat{u} + m\hat{v} + n\hat{w} \tag{2.11}$$

where $n = \sqrt{1 - l^2 - m^2}$. Inserting equations (2.10) and (2.11) into equation (2.9), and expanding $d\Omega$ out to get $d\Omega = dldm/\sqrt{1 - l^2 - m^2}$, we get

$$V = \iint I^t e^{\frac{-i\omega}{c}(\lambda u\hat{u} + \lambda v\hat{v})\cdot(l\hat{u} + m\hat{v} + n\hat{w})} \frac{dldm}{\sqrt{1 - l^2 - m^2}} \tag{2.12}$$

where we have temporarily written I as I^t, so that we can replace $I^t/\sqrt{1 - l^2 - m^2}$ with I, which is the true intensity function (I^t) projected onto the (l, m) plane. Noting that $\omega = 2\pi\nu$, where ν is the observed frequency, then we see that $\omega\lambda/c = 2\pi$. Putting all this into equation (2.12) we get

$$V(u, v) = \iint I(l, m) e^{-i2\pi(ul + vm)} dldm \tag{2.13}$$

Equation (2.13) above shows that the output of the correlator in an interferometer, the complex visibility function V, is a Fourier transform of the intensity distribution of the source in the sky.

2.2 Calibration

In equation (2.13) above, we wrote down an expression for the output of an interferometer called the visibility function V. In reality, however, the visibilities observed by an interferometer differ from the true visibilities due to atmospheric effects and anomalies in the electronics along the signal path of the interferometer. In order to extract the true visibilities from the observed visibilities, we make the assumption that they are related linearly for a pair of antennas so that

$$\bar{V}_{ij}(t) = g_i(t) g_j^*(t) V_{ij}^t(t) + \epsilon_{ij}(t) \tag{2.14}$$

where $\bar{V}_{ij}$ is the visibility function we observe, as opposed to V_{ij}^t which is the true visibility, g_i and g_j^* are the gains from the i^{th} and j^{th} antennas, and ϵ_{ij} is the thermal noise. The process of extracting the true visibilities from the observed visibilities is known as calibration.

2.2.1 Initial Calibration

The initial calibration of the data was carried out in Socorro NM by Emmanuel Momjian, a staff scientist at NRAO. After loading into the AIPS program, the data were inspected and any bad data that had not already been removed by the online processing system were flagged. The task SETJY was run to enter the intensity of the flux calibrator into a source (SU) table in the data. Every VLA observation is required to observe a standard source of known brightness in order to set the intensity scale. This is called the flux calibrator, and in these observations the source 3C147 was used. The tasks CALIB and CLCAL were then run in succession to propagate the intensity scale to the observed sources.

2.2.2 Self-Calibration

Since masers are compact and strong sources, we can use them to carry out our calibration. In this process known as self-calibration, we use an initial model of the maser visibilities to obtain our solutions for the gains and get a better measured set of visibilities from

$$\bar{V}_{ij}(t) = g_i(t) g_j^*(t) V_{ij}^{model}(t) + \epsilon_{ij}(t) \tag{2.15}$$

where V_{ij}^{model} are the model visibilities. Our initial model was obtained from an image of the peak maser in its strongest intensity channel. The procedure for obtaining images from calibrated visibilities with the task IMAGR is described in § 2.3. We used the task CALIB to do a least-squares fit to the visibility data to find the value of the gains in equation (2.15). We applied these gains to the data to obtain a new set of visibilities. We then used IMAGR to make a new model from these updated visibility data, and repeated the process of CALIB. This iterative process was repeated until there was little to no reduction in the rms flux density and no change in the peak maser intensity. At this stage, the calibrated visibilities are ready for final imaging.

2.3 Imaging

Upon inverting equation (2.13), we obtain an intensity image of the sky given by

$$I^d(l,m) = \iint V(u,v)\, e^{2\pi i(ul+vm)} du dv \tag{2.16}$$

where $V(u,v)$ are now the calibrated visibilities. Such an image is called a "dirty" image because it contains undesirable artifacts due to the fact that the Fourier plane is not completely sampled by the interferometer. To make this explicit, we introduce a sampling function $S(u,v)$ into equation (2.16), and assign $S(u,v) = 1$ at locations in the (u,v) plane that are sampled by the interferometer, and zero at all other points, so that

$$I^d(l,m) = \iint V(u,v)S(u,v)\, e^{2\pi i(ul+vm)} du dv \tag{2.17}$$

From the convolution theorem for Fourier transforms we get that

$$I^d(l,m) = I(l,m) * B(l,m) \tag{2.18}$$

where $B(l,m)$ is called the "dirty" beam and is given by the inverse Fourier transform of the sampling function

$$B(l,m) = \iint S(u,v)\, e^{2\pi i(ul+vm)} du dv \tag{2.19}$$

An example dirty beam from our observations is shown in Figure 2.3.

Equation (2.18) tells us that the dirty image is the desired image $I(l,m)$ convolved with the "dirty" beam. To obtain the desired image we have to deconvolve the dirty beam from the dirty image. In AIPS we use the task IMAGR for this process, which relies on the Clark-Högbom algorithm (Högbom 1974, Clark 1980). Each iteration of this algorithm picks out the point of highest intensity in the image and removes a portion of this strongest feature from the dirty image after convolving it with the dirty beam. For our purpose we removed 10% of the peak feature from the dirty image on each iteration. This is repeated until the strongest feature remaining in the dirty image is within a factor above the rms value for the noise. The algorithm keeps track of the intensities of each point identified in the dirty image, and produces the final clean image by convolving these points with a "clean" beam. The clean beam is obtained by fitting a (spatial) Gaussian function to the dirty beam. An example dirty image and clean image from our observations is shown in Figures 2.4 and 2.5, respectively.

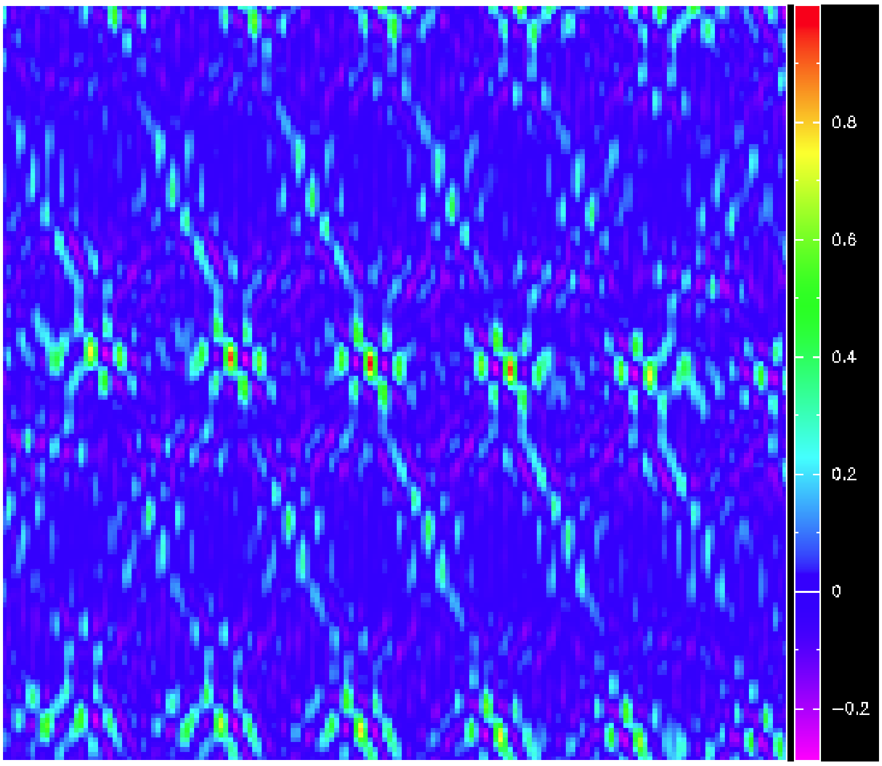

FIGURE 2.3: Figure showing an example dirty beam from our observations, constructed from the data for maser 3 in W41.

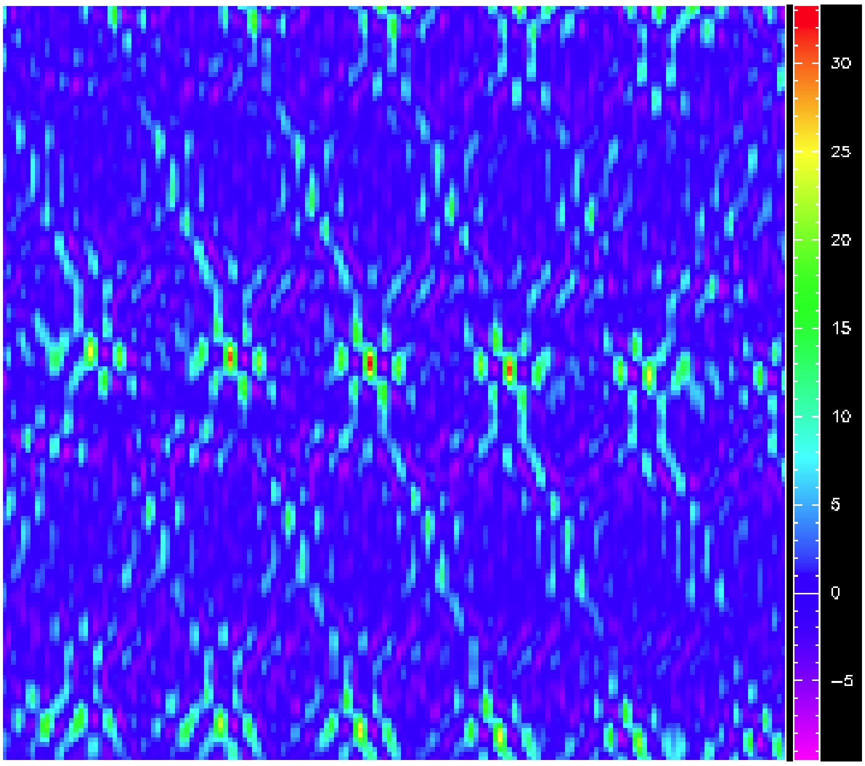

FIGURE 2.4: Figure showing an example dirty image from our observations, constructed from the data for maser 3 in W41.

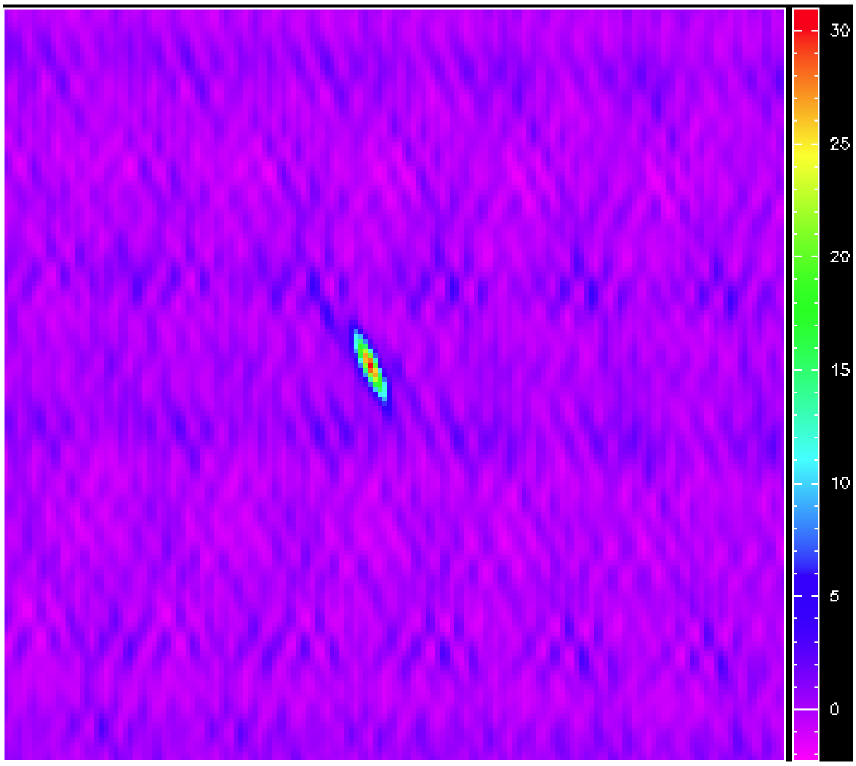

Figure 2.5: Figure showing an example clean image from our observations, constructed from the data for maser 3 in W41.

2.4 Our Observations and Data Reduction

The observations reported in this thesis were taken as part of VLA project AS 1022 (Principal Investigator A. Sarma) on July 10th, 17th, and 20th, 2010. Data for 7 star forming regions observed as part of this project are reported in this thesis. The positions of these regions that were pointed to by the VLA are given in Table 2.1, along with the time spent on each source (TOS).

Table 2.1: Table of Parameters for Observed Regions

Region Name	R.A. (J2000) (h:m:s)	Dec. (J2000) (° ′ ″)	TOS (sec)	Beam FWHM (″)	Beam PA (°)
S231	05:39:13.6	+36:45:51	339.0	2.346 × 1.636	35.4
W75N	20:38:36.8	+42:37:59	339.1	2.645 × 1.509	−20.6
W41	18:34:39.3	−08:31:39	314.1	7.643 × 1.662	24.2
W42	18:36:12.6	−07:12:11	309.2	3.983 × 1.448	−12.6
S255	06:12:54.2	+17:59:23	309.2	2.957 × 1.836	−39.8
23.01-0.41	18:34:40.4	−09:00:38	314.1	3.897 × 1.499	−11.7
29.86-0.04	18:45:59.5	−02:44:47	314.1	3.344 × 1.419	−5.0

While the descriptions in the above sections have all been for a single frequency, data for our observations were collected across many frequencies centered about the Doppler shifted frequency expected for the masers in each of the observed regions. Such frequencies are usually expressed as velocities by the Doppler shift equation

$$\frac{f - f_o}{f_o} = \frac{v}{c} \tag{2.20}$$

where f is the Doppler shifted frequency, f_o is the rest frequency of the observed maser line, v is the velocity, and c is the speed of light. In our case data were collected in 256 channels spanning a frequency bandwidth of 4000.0 kHz, giving a spectral resolution of 15.625 kHz. Converting this to velocities using equation (2.20) we get a velocity extent of 33.310 km s^{-1} across the entire bandwidth, corresponding to a velocity resolution of 0.13012 km s^{-1}. Therefore, the output of IMAGR after the deconvolution described in the previous section is a spectral cube containing 256 channels. Each channel of this cube is an image of the star forming region being observed. We have 7 data cubes, one for each star forming region. The parameters of the clean beam for each region are also given in Table 2.1.

We used the program AIPSVIEW to search for masers in each of the 7 data cubes. We looked through the image of each channel for maser features. When a possible maser feature showed up in a channel, we clicked on it to obtain its spectral profile, which is a plot of the intensity of the maser across all the channels. Since self-calibration removes all position information, the positions of these masers were recorded as offsets in right ascension and declination from the position of the highest intensity maser detected in that region. Finally, Gaussian profiles were fit to these maser spectra wherever possible, and their peak intensity, velocity of the peak (v_{LSR}), as well as the velocity width at half the peak maximum (Δv_{FWHM}) were recorded (Chapter 3).

Chapter 3

Results

In this chapter we present our results. In § 3.1, we present the line parameters for each maser from our Gaussian fits, and in § 3.2, we discuss the distribution of masers in each of the seven regions.

3.1 Maser Line Parameters

We detected twenty three 36 GHz Class I methanol masers in the seven star forming regions observed for this thesis. The largest number of masers (6) was observed in the star forming region S231, while two regions had only one maser each. The number of masers found in each of the 7 regions is given in Table 3.1. Each maser was fitted with a Gaussian profile. The parameters of the fitted Gaussians, namely the intensity, center velocity ($v_{\rm LSR}$), and velocity linewidth at half the maximum intensity ($\Delta v_{\rm FWHM}$) are also given in Table 3.1. Of the 7 regions, W41 has the highest intensity maser. For all the 5 regions with multiple masers per region, the spread in center velocities is not very large, the largest being 6.88 km s^{-1} for W42. All the masers have narrow line profiles with $\Delta v_{\rm FWHM}$ between 0.05 to 1.60 km s^{-1}.

Table 3.1: Parameters from Gaussian fits of 36 GHz methanol masers. The maser numbers correspond to the numbers seen in Appendix A.

Region	Maser Number	Intensity (Jy beam^{-1})	Center Velocity $v_{\rm LSR}$ (km s^{-1})	Velocity Width $\Delta v_{\rm FWHM}$ (km s^{-1})
S231	1	1.38 ± 0.06	−17.87 ± 0.01	0.77 ± 0.04
	2	1.73 ± 0.04	−16.75 ± 0.01	0.59 ± 0.01
	3	3.70 ± 0.05	−15.99 ± 0.01	0.45 ± 0.01
	4	0.91 ± 0.03	−15.54 ± 0.01	0.74 ± 0.03
	5	0.38 ± 0.02	−16.53 ± 0.03	1.60 ± 0.10
	6	0.55 ± 0.08	−19.72 ± 0.03	0.60 ± 0.10
W75N	1	0.88 ± 0.04	6.63 ± 0.01	0.43 ± 0.02
	2	0.93 ± 0.04	8.79 ± 0.01	0.31 ± 0.02
	3	1.07 ± 0.04	8.03 ± 0.01	0.53 ± 0.02
	4	2.03 ± 0.03	10.10 ± 0.01	0.45 ± 0.01
	5	0.51 ± 0.02	9.67 ± 0.01	0.75 ± 0.04
W41	1	11.20 ± 0.40	96.65 ± 0.01	0.83 ± 0.04
	2	24.70 ± 0.30	102.67 ± 0.01	1.20 ± 0.02
	3	31.80 ± 0.30	99.63 ± 0.01	0.39 ± 0.01
	4	26.00 ± 0.40	101.30 ± 0.01	0.44 ± 0.01
W42	1a	4.63 ± 0.06	113.91 ± 0.01	0.11 ± 0.01
	1b	1.87 ± 0.06	113.19 ± 0.01	0.05 ± 0.01
	1c	1.27 ± 0.06	112.64 ± 0.02	0.05 ± 0.01
	2	14.20 ± 0.10	114.81 ± 0.01	0.62 ± 0.01
	3	2.69 ± 0.08	107.93 ± 0.01	0.53 ± 0.02
	4a	7.40 ± 0.10	109.78 ± 0.01	0.11 ± 0.01
	4b	3.50 ± 0.10	110.00 ± 0.01	0.05 ± 0.01
	4c	1.35 ± 0.07	111.83 ± 0.02	0.05 ± 0.01
S255	1	1.91 ± 0.07	9.96 ± 0.01	0.55 ± 0.02
	2	0.47 ± 0.06	11.20 ± 0.02	0.50 ± 0.08
23.01-0.4	1	7.00 ± 0.20	77.15 ± 0.01	0.72 ± 0.02
29.86-0.04	1a	1.95 ± 0.02	99.49 ± 0.01	0.50 ± 0.01
	1b	0.81 ± 0.02	99.04 ± 0.01	0.50 ± 0.01

3.2 Discussion of Regions

We will now discuss each of the 7 regions individually.

3.2.1 Region S231

We observed the largest number of masers in S231. The spatial distribution of the 6 masers observed in this region is given in Figure 3.1. The distribution shows some signs of clustering. Masers 1 and 6 in the southwest (bottom right) are very close to each other at $0.07^{\rm s}$ (equivalent to $0.79''$) apart. Similarly masers 3, 4, and possibly 5 in the southeast could be part of the same cluster. We will look at the possible meaning behind these clusters in § 4.4.

The strongest maser in S231 is maser 3 (Figure 3.1) with an intensity of 3.70 Jy beam^{-1} and a center velocity of $v_{\rm LSR} = -15.99$ km s^{-1}. The velocity profiles and Gaussian fits for each maser can be seen in Appendix A.1. The center velocities of the 6 masers range from -19.72 to -15.54 km s^{-1}. The maser lines are quite narrow, with velocity linewidths ranging from 0.45 to 1.60 km s^{-1}. Masers 2, 3, 4, and 5 each have only one velocity component, but masers 1 and 6 display two velocity components (Figures A.1 and A.6 respectively). This is merely due to the two maser spots being so close to each other. They would be spatially unresolved in our observations; their separation of 0.79″ is smaller than the synthesized beam width in Table 2.1. However, because their profiles peak at different velocities, it is possible to tell that there are two maser spots. Still, since they are unresolved, each spot contains the velocity profile of the other, except at a lower intensity. Therefore, in Figures A.1 and A.6, we have fitted for only one velocity component for masers 1 and 6.

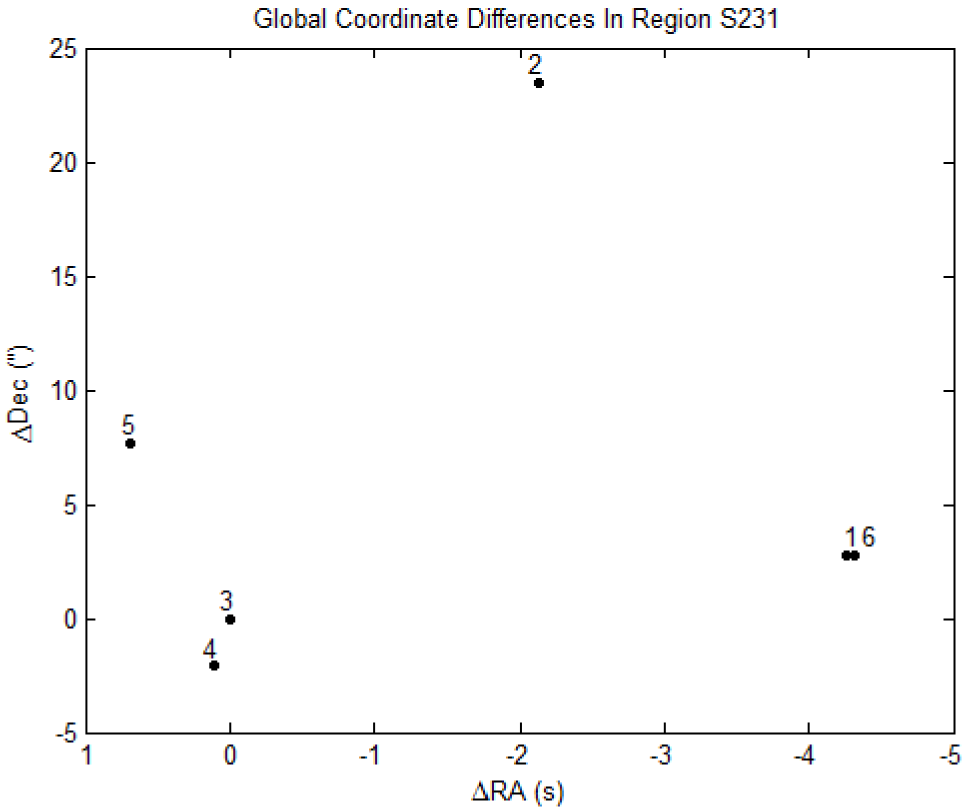

FIGURE 3.1: Plot of the distribution of 36 GHz masers in the star forming region S231. The (0,0) position in the figure is the location of the strongest maser in this source (maser 3 in Table 3.1).

3.2.2 Region W75N

We observed 5 masers in W75N; their spatial distribution is given in Figure 3.2. Masers 1, 2, 3, and 4 are arranged in a curved shape in the north-east (top left) corner. This could be indicative of a bow shock as an outflow encounters the surrounding molecular cloud. In addition to this, the four masers in the northeast and maser 5 in the southwest are along a linear structure as expected for a well collimated outflow with a small opening angle. We will look at both of these possibilities in § 4.4. The strongest maser in W75N is maser 4 with an intensity of 2.03 Jy beam^{-1} and a center velocity of $v_{\rm LSR}$ = 10.10 km s^{-1}. As in S231, the center velocities of the 5 masers span a small range from 6.63 to 10.10 km s^{-1}. The five maser spots each have a single narrow velocity component, with velocity linewidths ranging from 0.31 to 0.75 km s^{-1}. The velocity profiles and Gaussian fits for each maser can be seen in Appendix A.2.

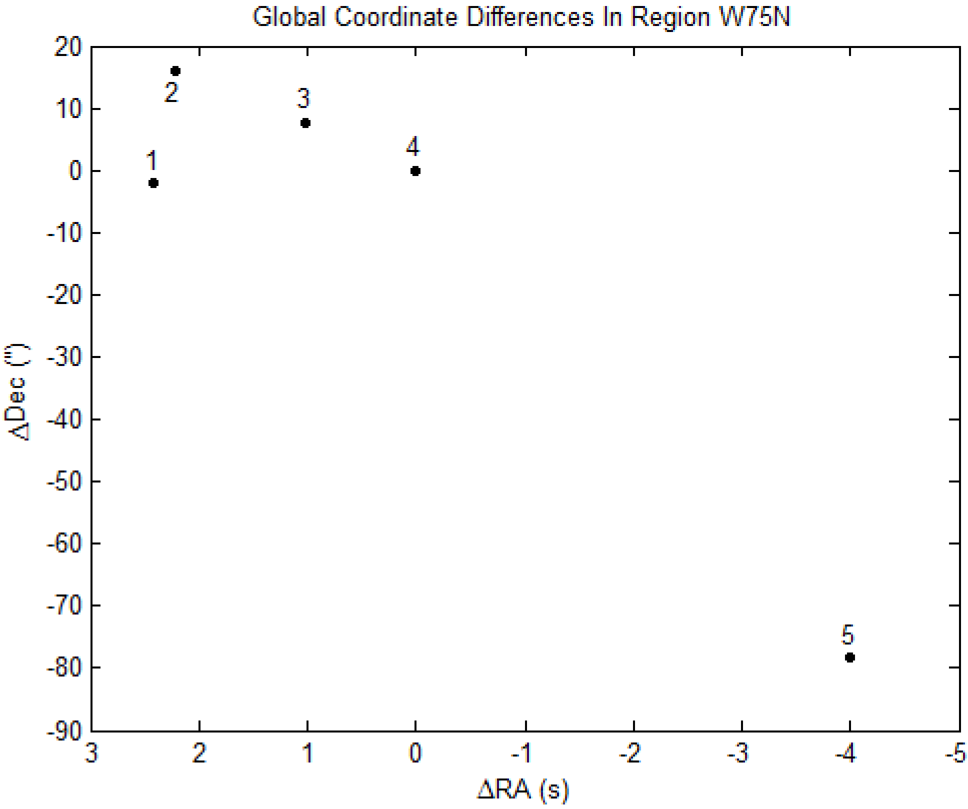

FIGURE 3.2: Plot of the distribution of 36 GHz masers in the star forming region W75N. The (0,0) position in the figure is the location of the strongest maser in this source (maser 4 in Table 3.1).

3.2.3 Region W41

Among the seven regions reported in this thesis, W41 had the masers with the highest intensity. The strongest maser in W41 with an intensity of 31.80 Jy beam^{-1} was the most intense 36 GHz maser in our survey. The spatial distribution of the 4 masers observed in this region is given in Figure 3.3, and the velocity profiles and Gaussian fits for each maser can be seen in Appendix A.3. Given the presence of such strong masers so close to each other, contamination from the profile of one maser can be seen in the other maser profiles. For example, in the profile for maser 4 in Figure A.14 which peaks at a center velocity of 101.30 km s^{-1}, we see a kink near 99.63 km s^{-1}, the center velocity of the strongest maser 3. Likewise, in the profile of maser 2 which peaks at 102.67 km s^{-1} (Figure A.13), we see a kink near 101.30 km s^{-1}, the velocity at which maser 4 has its peak. The case is even more extreme for maser 1, which has the lowest intensity of the four masers in W41. In Figure A.12, we not only see kinks near 102.67 km s^{-1} and 101.30 km s^{-1} (the center velocities of masers 2 and 4, respectively), but we also have a significant residual spike of 8 Jy beam^{-1} at 99.63 km s^{-1}, the center velocity of the strongest maser 3. Like S231 and W75N, though, the profiles of the 4 masers in W41 are also quite narrow, with velocity linewidths ranging from 0.39 to 1.20 km s^{-1}.

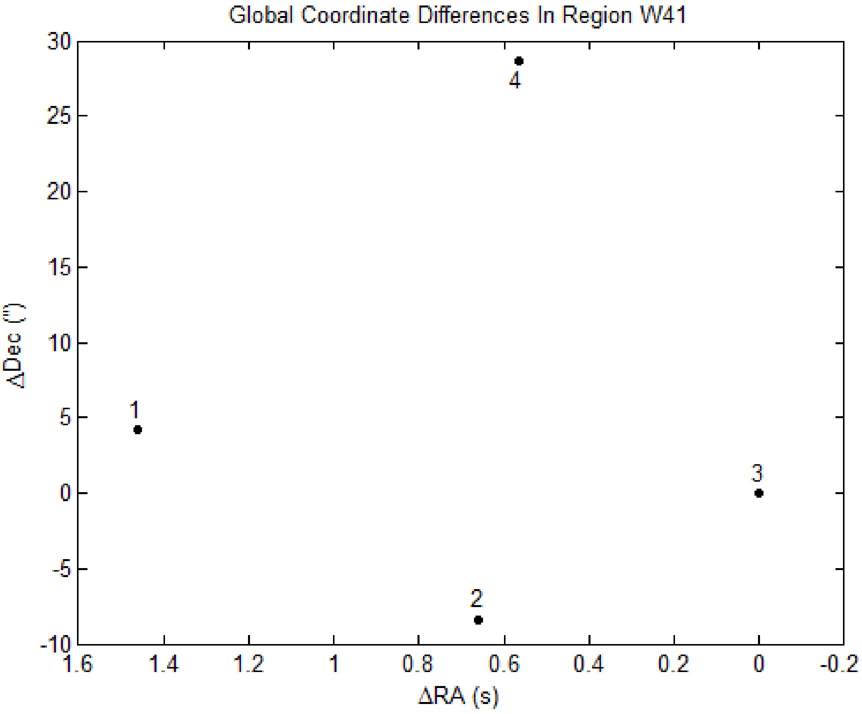

Figure 3.3: Plot of the distribution of 36 GHz masers in star forming region W41. The (0,0) position in the figure is the location of the strongest maser in this source (maser 3 in Table 3.1).

3.2.4 Region W42

We observed 4 masers in W42, and their spatial distribution is shown in Figure 3.4. The velocity profiles and Gaussian fits for each maser can be seen in Appendix A.4. The strongest maser in this region, maser 2, has a single velocity component with center velocity at 114.81 km s^{-1} and an intensity of 14.20 Jy $beam^{-1}$, as does maser 3. Masers 1 and 4, though, each have three velocity components. Each of these components are likely real, since they do not correspond to the center velocities of any other masers in the field. Most likely, they each correspond to three unresolved maser spots that are near enough in center velocity that we do not see them as adjacent spots, unlike masers 1 and 6 of S231. Therefore, we have fitted them with 3-component Gaussians (Table 3.1). Each of the fitted profiles for masers 1 through 4, including the single components for 2 and 3 and the three components each for 1 and 4, are however quite narrow, with velocity linewidths ranging from 0.05 to 0.62 km s^{-1}.

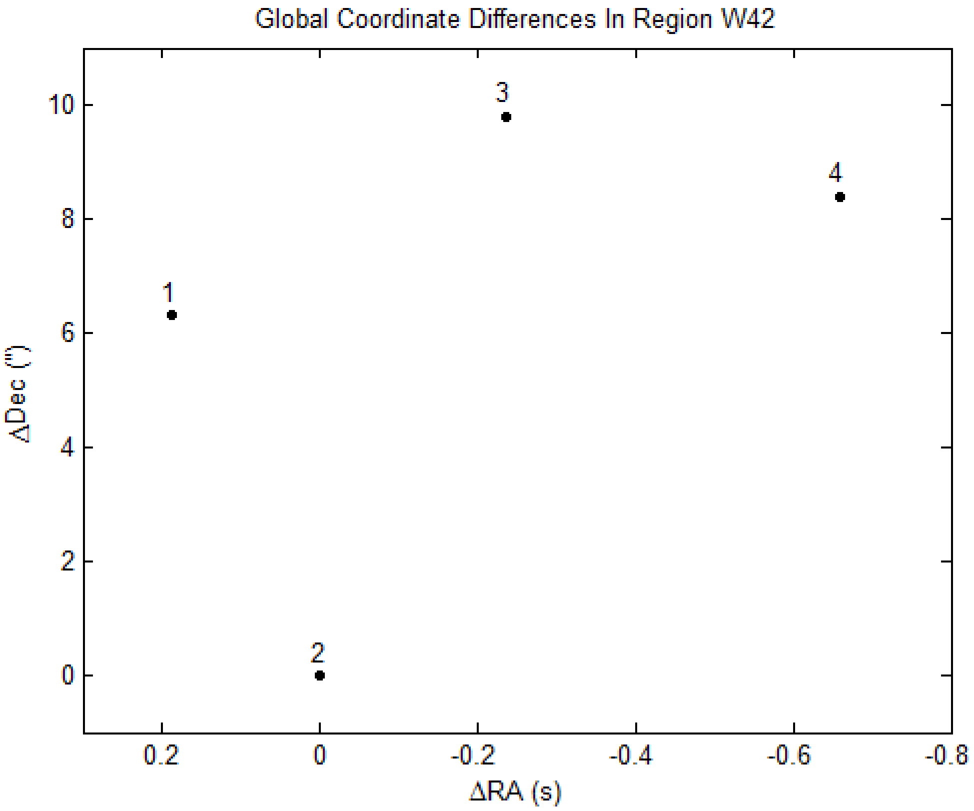

FIGURE 3.4: Plot of the distribution of 36 GHz masers in the star forming region W42. The (0,0) position in the figure is the location of the strongest maser in this source (maser 2 in Table 3.1).

3.2.5 Region S255

We observed only 2 masers in S255. The spatial distribution of these 2 masers is given in Figure 3.5, and their velocity profiles and Gaussian fits can be seen in Appendix A.5. The two masers are arranged along a northwest to southeast line that is consistent with being on the opposite ends of an outflow; however, two masers are not sufficient to constrain a particular geometry. The two masers each have only one velocity component that is quite narrow with a linewidth ∼ 0.5 km s^{-1}, and the center velocities are not too far apart at 9.96 and 11.20 km s^{-1} respectively. The intensity of maser 2 is only about a third that of the stronger maser 1.

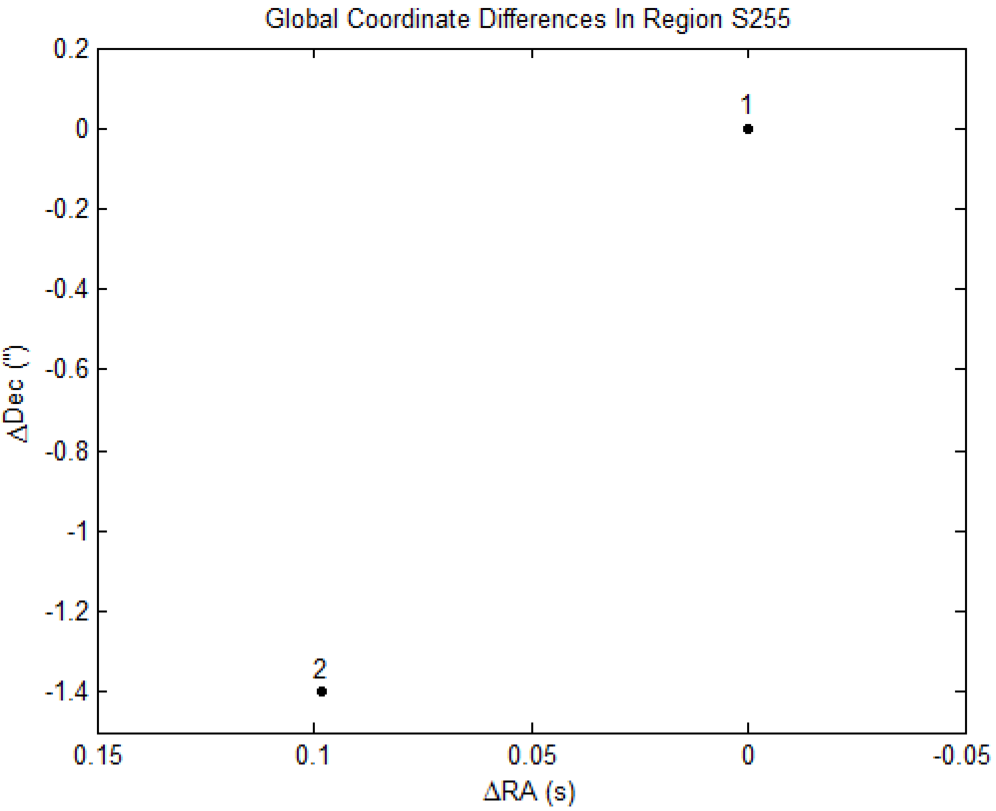

FIGURE 3.5: Plot of the distribution of 36 GHz masers in the star forming region S255. The (0,0) position in the figure is the location of the strongest maser in this source (maser 1 in Table 3.1).

3.2.6 Region 23.01-0.4

We observed only 1 maser in 23.01-0.4; its velocity profile and Gaussian fit can be seen in Appendix A.6.. The maser had an intensity of 7.00 Jy beam^{-1}, a center velocity of $v_{\text{LSR}} = 77.15$ km s^{-1}, and a narrow velocity linewidth of 0.72 km s^{-1}.

3.2.7 Region 29.86-0.04

In 29.86-0.04, we also observed only 1 maser, but it had two velocity components separated by only 0.45 km s^{-1}. The velocity profile and Gaussian fit can be seen in Appendix A.7. Both velocity components are narrow with a linewidth of 0.50 km s^{-1}, but the intensity of the weaker component is less than half that of the stronger component. The situation is similar to masers 1 and 4 in W42, in that we likely have two unresolved maser spots in 29.86-0.04 that are near enough in center velocity that we do not see them as adjacent spots.

Chapter 4

Discussion and Analysis

In this chapter we compare the results of our 36 GHz Class I methanol maser observations with 6.7 GHz Class II masers taken from the literature. In § 4.1, we compare the intensities of our observed 36 GHz masers and 6.7 GHz masers. In § 4.2, we compare the center velocities of these classes of masers. In § 4.3, we explore connections between these classes of masers based on a quantity called the profile difference. In § 4.4, we look in more detail at three regions for which there are high angular resolution 6.7 GHz methanol maser observations in the literature.

4.1 Analysis of Maser Intensities

First we will compare the intensities of the 36 GHz Class I masers and the intensity of the 6.7 GHz Class II maser in each region. Table 4.1 shows the data for all the 36 GHz masers that we observed in each region (taken from Table 3.1) and for 6.7 GHz masers from the literature. The references for the 6.7 GHz masers can be found in Appendix B.1.

Table 4.1: Table showing the data for 36 GHz masers and the 6.7 GHz masers found in each region.

	36 GHz Masers				6.7 GHz Masers		
Region	Maser Number	Intensity (Jy beam^{-1})	v_{LSR} (km s^{-1})	Δv_{FWHM} (km s^{-1})	Intensity (Jy)	v_{LSR} (km s^{-1})	Δv_{FWHM} (km s^{-1})
S231	1	1.38 ± 0.06	-17.87 ± 0.01	0.77 ± 0.04	208	-12.8	1.5
	2	1.73 ± 0.04	-16.75 ± 0.01	0.59 ± 0.01			
	3	3.70 ± 0.05	-15.99 ± 0.01	0.45 ± 0.01			
	4	0.91 ± 0.03	-15.54 ± 0.01	0.74 ± 0.03			
	5	0.38 ± 0.02	-16.53 ± 0.03	1.60 ± 0.10			
	6	0.55 ± 0.08	-19.72 ± 0.03	0.60 ± 0.10			
W75N	1	0.88 ± 0.04	6.63 ± 0.01	0.43 ± 0.02	1080	7.12	0.4
	2	0.93 ± 0.04	8.79 ± 0.01	0.31 ± 0.02			
	3	1.07 ± 0.04	8.03 ± 0.01	0.53 ± 0.02			
	4	2.03 ± 0.03	10.10 ± 0.01	0.45 ± 0.01			
	5	0.51 ± 0.02	9.67 ± 0.01	0.75 ± 0.04			
W41	1	11.20 ± 0.40	96.65 ± 0.01	0.83 ± 0.04	42.1	103.2	16
	2	24.70 ± 0.30	102.67 ± 0.01	1.20 ± 0.02			
	3	31.80 ± 0.30	99.63 ± 0.01	0.39 ± 0.01			
	4	26.00 ± 0.40	101.30 ± 0.01	0.44 ± 0.01			
W42	1a	4.63 ± 0.06	113.91 ± 0.01	0.11 ± 0.01	82	108.6	8
	1b	1.87 ± 0.06	113.19 ± 0.01	0.05 ± 0.01			
	1c	1.27 ± 0.06	112.64 ± 0.02	0.05 ± 0.01			
	2	14.20 ± 0.10	114.81 ± 0.01	0.62 ± 0.01			
	3	2.69 ± 0.08	107.93 ± 0.01	0.53 ± 0.02			
	4a	7.40 ± 0.10	109.78 ± 0.01	0.11 ± 0.01			
	4b	3.50 ± 0.10	110.00 ± 0.01	0.05 ± 0.01			
	4c	1.35 ± 0.07	111.83 ± 0.02	0.05 ± 0.01			
S255	1	1.91 ± 0.07	9.96 ± 0.01	0.55 ± 0.02	72	4.62	0.4
	2	0.47 ± 0.06	11.20 ± 0.02	0.50 ± 0.08			
23.01-0.4	1	7.00 ± 0.20	77.15 ± 0.01	0.72 ± 0.02	405	74.8	3
29.86-0.04	1a	1.95 ± 0.02	99.49 ± 0.01	0.50 ± 0.01	67	101.4	1
	1b	0.81 ± 0.02	99.04 ± 0.01	0.50 ± 0.01			

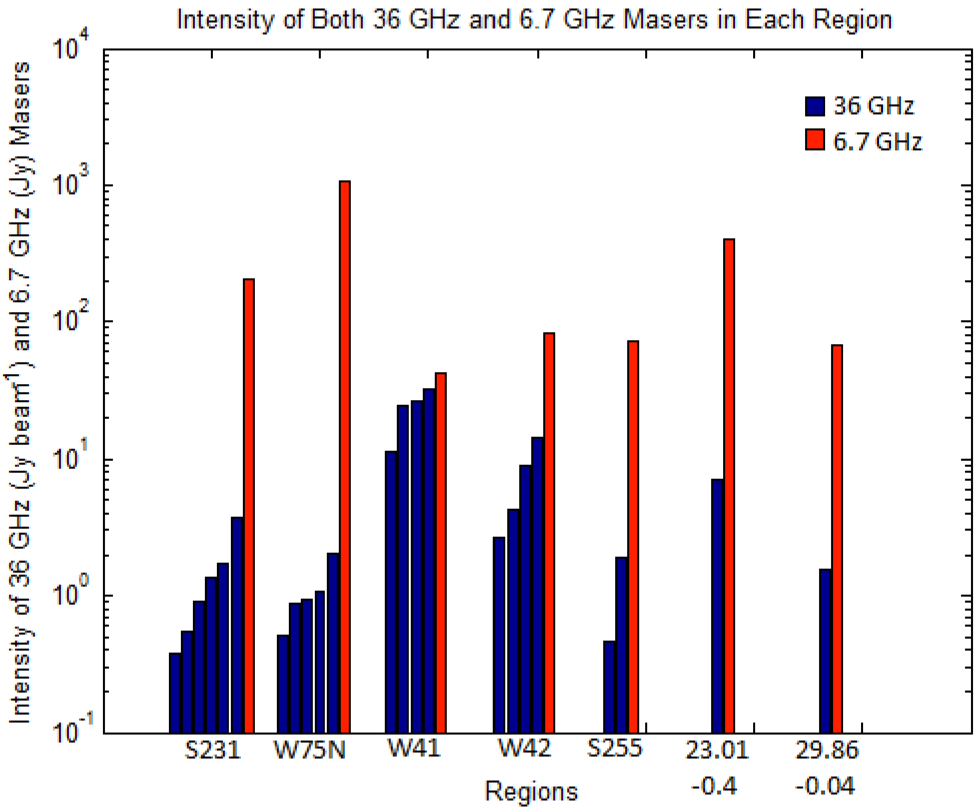

FIGURE 4.1: Plot comparing the intensities of 36 GHz masers and their associated 6.7 GHz masers. Note that the vertical axis is on a logarithmic scale, e.g., the 6.7 GHz maser in W75N is 500 times brighter than the strongest 36 GHz maser in that region.

When comparing the peak intensities of the 36 GHz masers to their associated 6.7 GHz masers both in Figure 4.1 and Table 4.1, we see signs of anti-correlation in that regions containing high intensity 6.7 GHz masers generally have relatively low intensity 36 GHz masers. For example, the 6.7 GHz peak intensity in S231 is 208 Jy, whereas the strongest 36 GHz maser in this region is only 3.70 Jy beam^{-1}. Meanwhile, the 6.7 GHz maser in the region W75N is over a factor of 500 stronger than the highest intensity 36 GHz maser in that region. The only exception is W41, where the 6.7 GHz peak intensity is comparable to the peak intensity of all the four 36 GHz masers in that region. Because the 6.7 GHz masers were observed with single dish telescopes, it is possible that their high intensity is caused by multiple unresolved masers adding together. Even so, it is still the case that the 6.7 GHz intensity will likely be higher than the 36 GHz intensity. When Surcis et al. (2009) observed 6.7 GHz methanol masers with the European VLBI network (EVN), they found a total of 10 masers in W75N, with the highest maser having an intensity of 107 Jy. If we were able to do very long baseline interferometry (VLBI) for our 36 GHz masers, the W75N maser intensities would be much less than the 2 Jy maximum that we have observed with the VLA for this region. Of course, our claim that regions containing strong 6.7 GHz methanol masers appear to be associated with much weaker 36 GHz masers must be considered speculative at this time because our sample is so small. This anti-correlation between 36 GHz Class I and 6.7 GHz Class II methanol maser intensities is consistent with a similar anti-correlation between 44 GHz Class I and 6.7 GHz Class II methanol masers found by Slysh et al. (1994). On the other hand, Ellingsen et al. (2004) found a correlation between 95 GHz Class I and 6.7 GHz Class II methanol masers. These seemingly conflicting results point to the complexity of the methanol molecule's possible transitions and the need for theoretical studies of methanol maser pumping and propagation models.

We speculate that the anti-correlation we have discovered (of weak 36 GHz masers at strong 6.7 GHz sites) might be because these two maser classes occur at different epochs of the star forming regions in which they are found. Our speculation is based on the fact that these two classes of masers are pumped by different means (collisionally for 36 GHz Class I and radiatively for 6.7 GHz Class II) in different spatial regions. That is, we believe based on our findings that the regions we have observed are those in which radiative processes have begun to dominate and are creating strong 6.7 GHz Class II methanol masers, and the collisional processes are not as strong as they were in an earlier stage of these regions, so the 36 GHz Class I methanol masers we have observed are weaker. This seems to agree with the findings of Pratap et al. (2008): "In sources with evidence of very young star formation or with no obvious evidence of protostellar activity, the 36 GHz line emission is enhanced...," whereas radiative processes would not begin to dominate until later.

4.2 Analysis of Maser Velocities

Figure 4.2 shows the difference between the center velocities (v_{LSR}) of 36 GHz Class I masers and the v_{LSR} of their associated 6.7 GHz Class II masers. Comparing the v_{LSR} of each 36 GHz maser to their associated 6.7 GHz maser, we see that they are quite close to each other, with the smallest difference in velocities near 0.5 km s^{-1}, and the largest near 7 km s^{-1}. For example, in W75N maser 1 has a v_{LSR} of 6.63 km s^{-1} and the 6.7 GHz maser has a v_{LSR} of 7.12 km s^{-1}, showing a difference of only 0.49 km s^{-1}. There are other regions in which 36 GHz masers show small velocity differences with their associated 6.7 GHz masers, such as 0.53 km s^{-1} in W41 for maser 2 and 0.67 km s^{-1} in W42 for maser 3. On the other hand, at least one maser in S231, W41, W42, and S255 has its v_{LSR} at least 6 km s^{-1} away from the 6.7 GHz center velocity. Still, even a 6 km s^{-1} difference in center velocities is surprisingly small compared to the spreads in center velocities of H_2O masers, which can be upward of 30 km s^{-1} in many cases.

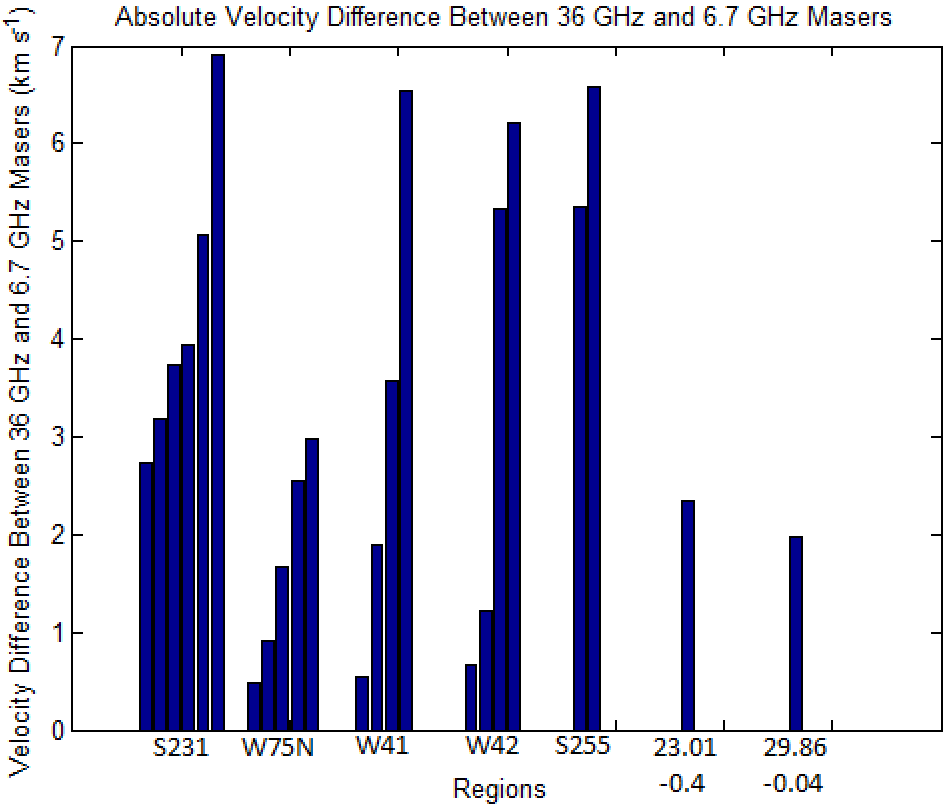

FIGURE 4.2: Graph showing the absolute difference between the $v_{\rm LSR}$ values of the 36 GHz Class I maser in each region with their associated 6.7 GHz Class II maser.

We can also compare the $v_{\rm LSR}$ of the 36 and 6.7 GHz masers to the systemic velocity of the region. The systemic velocity of a region is the Doppler shifted velocity of the region due to its location in the Galaxy, and can usually be determined using thermal molecular lines. The systemic velocities of the seven regions we observed are listed in Table B.2. Figure 4.3 shows a plot of the absolute difference between the $v_{\rm LSR}$ of the 36 GHz masers and the systemic velocity for each of the 7 regions, and a similar difference between the $v_{\rm LSR}$ of the 6.7 GHz maser and systemic velocity for those regions. We see that in all of the 7 regions the $v_{\rm LSR}$ of one or more of the 36 GHz masers is closer to the systemic velocity of that region than the $v_{\rm LSR}$ of the 6.7 GHz maser in that region. It is not a surprise that the 6.7 GHz maser velocities are offset from the systemic velocity since they are likely taking part in the motions of the disk around the protostar. For example, Surcis et al. (2009) found from their VLBI observations that the 6.7 GHz masers in W75N are located in filamentary structures, and interpreted them to be part of a rotating or expanding disk. From this, one would expect the velocities of the 6.7 GHz masers to be different from the systemic velocities of the cloud. What is surprising is that some of the 36 GHz maser velocities are so close to the systemic velocity; for example, in S231 maser 2 has a difference of 0.05 km s^{-1} and in W41 maser 3 has a difference of 0.2 km s^{-1} from the systemic velocity. This is either a random coincidence, or it is possible that these 36 GHz masers lie at the base of the outflow. However, none of our current observations has enough masers to allow us to distinguish between these two possibilities.

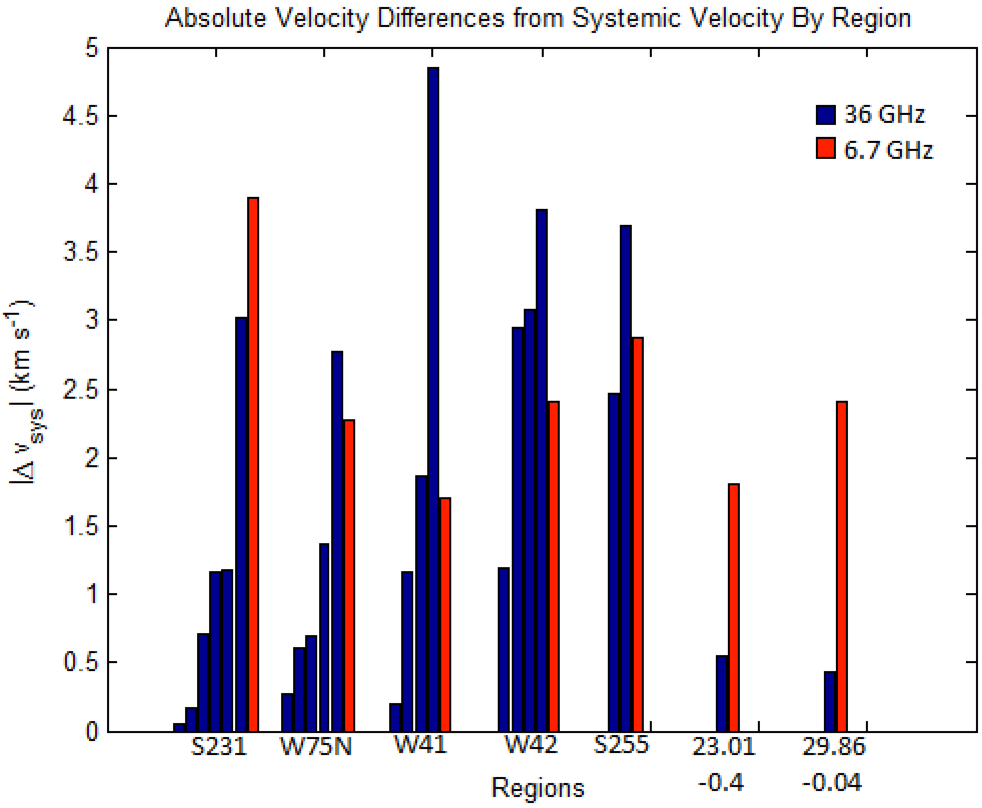

FIGURE 4.3: Graph showing the absolute difference between the v_{LSR} values of each maser and the systemic velocity of the region. A bar of lower height indicates that the v_{LSR} of that maser is closer to the systemic velocity.

4.3 Analysis of Connections

In this section, we will look at the differences in velocity profiles as a whole, combining the center velocity (v_{LSR}) value, the full-width at half maximum (FWHM) of the profile, and the peak intensity. We will focus much of our velocity discussion on the "profile difference" which is defined as

$$\Delta v_p = |\Delta v| - \frac{1}{2}(FWHM_{36} + FWHM_{6.7}) \tag{4.1}$$

where $|\Delta v|$ is the absolute velocity difference between the v_{LSR} of the two classes of masers, and FWHM$_{36}$ and FWHM$_{6.7}$ are the FWHM's for the 36 GHz maser and 6.7

GHz maser, respectively. Equation 4.1 tells us that negative differences have overlap between the two profiles, implying a likely spatial connection. An example of what these numbers show for velocity profiles can be seen in Figure 4.4, which shows two ideal Gaussians that have a zero profile difference. While it may seem that this shows little overlap, this will still show a shared velocity range above the noise. There is also precedent for using this type of velocity analysis in other similar surveys such as in Ellingsen et al. (2004).

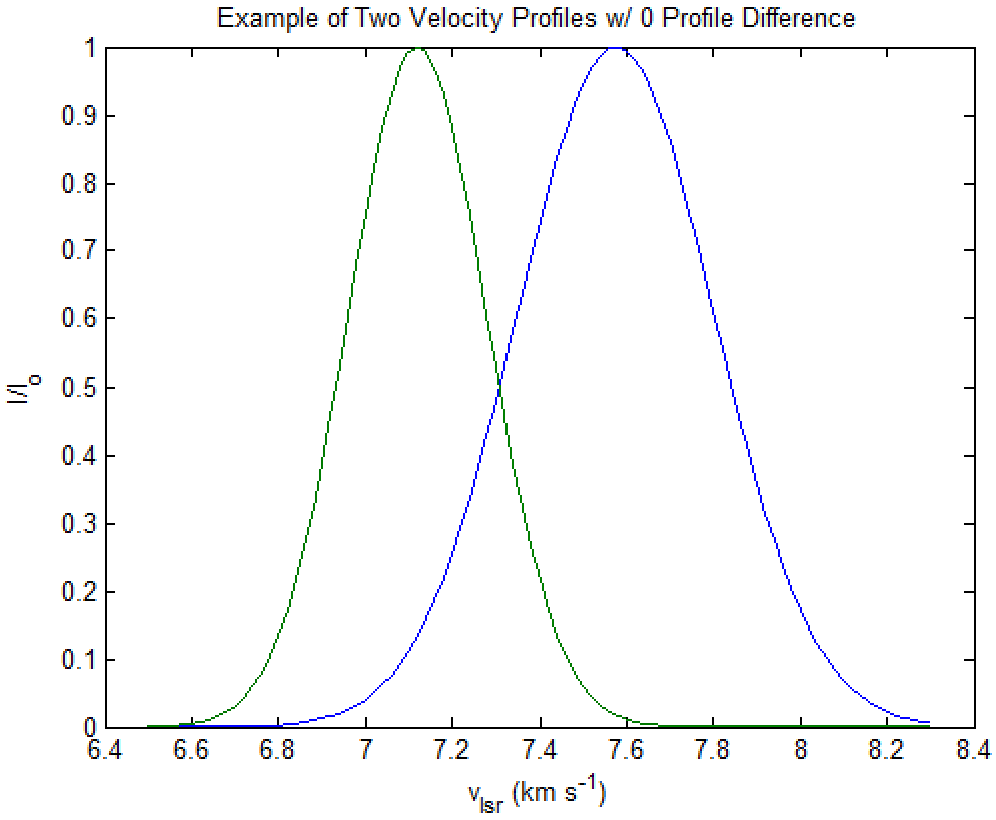

FIGURE 4.4: Plot of two Gaussian profiles with v_{LSR} and FWHM values that would give a profile difference value of zero.

In Figure 4.5 we compare the intensity of the observed 36 GHz masers with their associated profile difference (Δv_p) values. We see that 36 GHz masers which have larger negative Δv_p with their associated 6.7 GHz masers also have higher intensities. On the other hand, we see no such grouping if we plot the intensities of 36 GHz masers against the difference of their v_{LSR} from the systemic velocity of the region, as we have done in Figure 4.6. Figure 4.5 suggests that the intensity of the 36 GHz maser may be correlated to the amount of overlap (seen by more negative velocity differences indicating more overlap). We conclude that, assuming profile difference gives information on spatial connections, higher intensity 36 GHz masers are closer to 6.7 GHz masers.

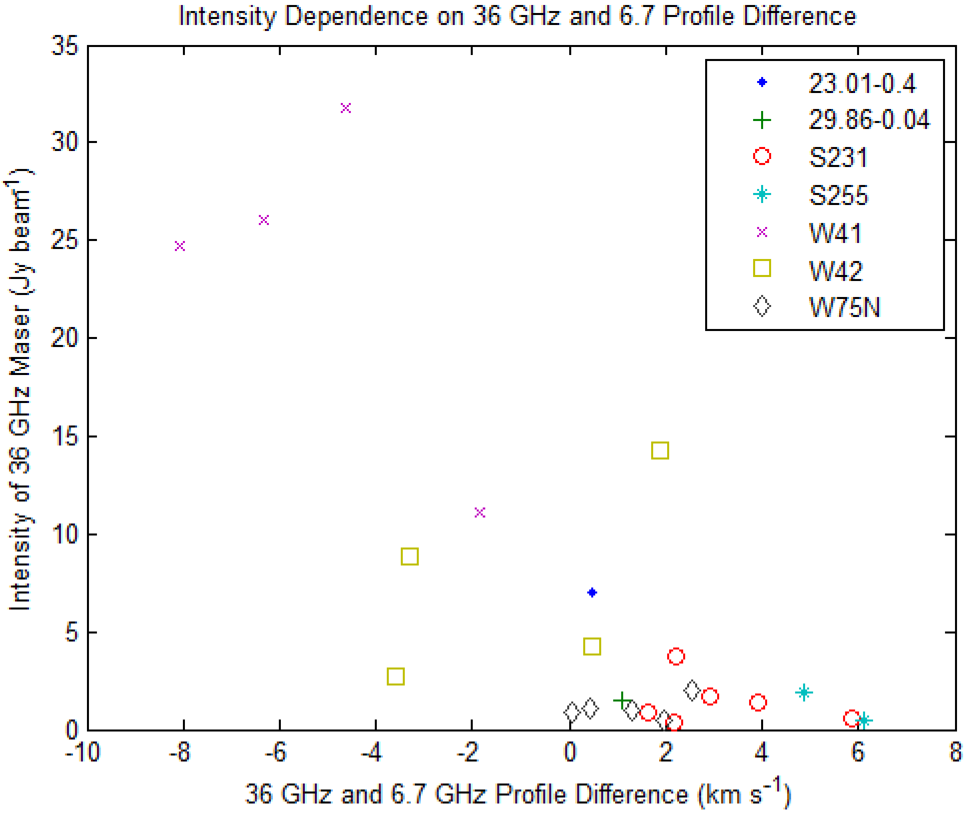

FIGURE 4.5: Plot comparing the intensities of 36 GHz masers and their profile differences with 6.7 GHz masers. The profile difference is defined in § 4.3.

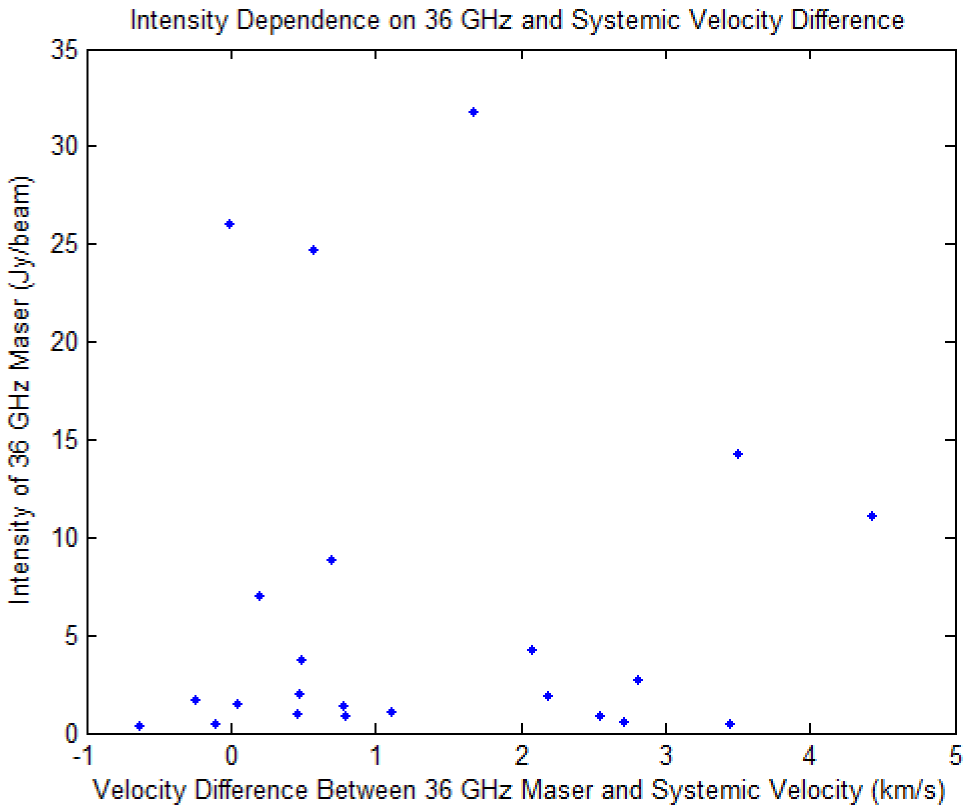

Figure 4.6: Plot comparing the intensities of 36 GHz masers and the velocity difference from their associated cloud's systemic velocity.

4.4 Discussion of Individual Regions

In this section, we will look at three of the seven star forming regions in more detail. We chose these regions because there are existing high angular resolution observations of 6.7 GHz Class II masers in the literature for each of these three regions. We will compare these high angular resolution 6.7 GHz observations in the literature to the distribution of 36 GHz Class I masers that we observed, as well as incorporate information about known outflows and continuum data.

4.4.1 W75N

Figure 4.7 shows the distribution of 36 GHz masers in W75N from our observations (taken from Figure 3.2) in the panel on the upper left, along with other associated features of interest. The top right panel, from Shepherd et al. (2003), shows a contour map in the CO emission line and is approximately the same size as our observed distribution. Mapping the intensity of this emission line is a common way to find the direction of outflows from protostars. Since we have lost absolute positional data in the self-calibration process we cannot be sure how our distribution of 36 GHz masers maps onto the CO emission map. However, it is clear that the northeast-southwest line of our 36 GHz maser distribution is oriented along the direction of the CO outflow. Moreover, the curve in the northeast (top left) of our 36 GHz maser distribution agrees with the basic morphology of a bow shock that would be created when ambient molecular material was shocked by the CO outflow depicted in the upper right panel.

The two images in the bottom panel of Figure 4.7 show a much smaller scale view of the region. The scale for the bottom left image, from Surcis et al. (2009), is shown as the inset box in our observed distribution (upper left panel). Even though we have no position information from our observations, we have chosen to put this inset box at the center of our distribution, as a hypothesized location of the central protostar. The bottom left panel in Figure 4.7 shows a map of 6.7 GHz masers in red, H_2O masers in blue, 1.3 cm continuum contour lines, and arrows in the direction of the observed outflow. The 1.3 cm continuum contours locate two separate star forming regions labeled VLA 1 and VLA 2. Surcis et al. (2009) found that VLA 1 has a linear formation of 6.7 GHz masers associated with it, labeled A1-A5. The 6.7 GHz masers labeled C1-C4 form an arc and may be associated with VLA 1, VLA 2, or a third star forming region that does not have an associated continuum source (which would mean that it is in an even earlier stage of formation than VLA 1 and VLA 2).

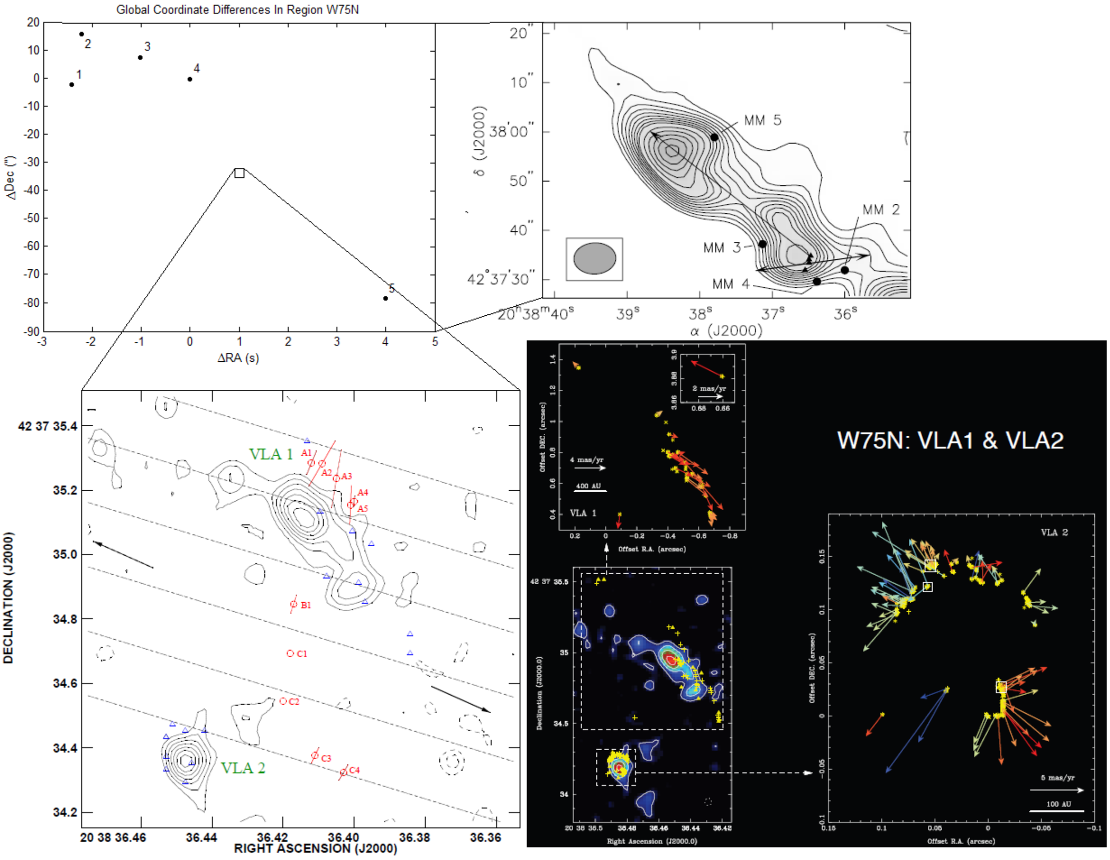

FIGURE 4.7: Plot showing the distribution of 36 GHz masers in W75N in reference to other known features. The distribution of 36 GHz masers from the observations reported in this thesis is shown in the upper left panel (taken from Figure 3.2). In the upper right panel is a CO image of the large scale outflow in this region from Shepherd et al. (2003) on the same scale as the image in the upper left panel. The distribution of 6.7 GHz Class II masers (red open circles), together with 1.3 cm continuum contours and H_2O masers (blue triangles), is shown in the bottom left panel (Surcis et al. 2009, and references therein). The image in the bottom right panel shows an enlarged view of the H_2O masers associated with the continuum sources VLA 1 and VLA 2, and a plot of the proper motions of these masers (Torrelles et al. 2012). While we do not have absolute position information for our 36 GHz masers, the direction of the outflow lines up well with the 36 GHz maser distribution.

The image in the bottom right panel, from Torrelles et al. (2012), is an enlarged view of VLA 1 and VLA 2 showing the H_2O masers associated with these two regions. Also shown are maps of the proper motions (in the plane of the sky) of some of these H_2O masers. Based on the smaller angular spread of the proper motion vectors of the H_2O masers associated with VLA 1 as opposed to the larger angular spread in proper motion vectors for VLA 2, Torrelles et al. (2012) concluded that VLA 1 is a more evolved region with a better collimated outflow.

From the above discussion, we see the potential of high angular resolution 36 GHz maser observations. Already from our pilot observation, we have established that the observed

36 GHz masers trace a bow shock in an outflow. Follow-up observations, especially with position information, might help to establish the evolutionary status of the star forming regions VLA 1 and VLA 2, set up closer connections with 6.7 GHz Class II masers, and with larger scale tracers of the region (like the CO line data).

4.4.2 S231

Figure 4.8 shows the distribution of 36 GHz masers that we observed in S231 (taken from Figure 3.1) in the upper left panel. The panel on the right shows a map of H_2 emission taken from Ginsburg et al. (2009), with proposed outflows marked with arrows. The scale of our observed distribution is shown in the inset box in the right panel, although the position of the inset in the region is completely speculative since we do not have any position information. However, our observed distribution is consistent with the general direction of some of the outflows marked in the right panel. With absolute positional data we would be able to correlate our observed masers to these outflows.

The bottom panel in Figure 4.8, taken from Minier et al. (2000), shows a map of 6.7 GHz masers in the region. The approximate scale of this map is shown in the inset box for the observed 36 GHz maser distribution, and again we have chosen to set the inset box at the center of the distribution of our observed masers, even though we have no knowledge of its actual position. The 6.7 GHz masers trace linear formations, which might correlate to the accretion disks surrounding the protostar(s). Further study could reveal a self-consistent picture of 6.7 GHz masers tracing the accretion disk and 36 GHz masers tracing the outflows in this and similar regions.

4.4.3 S255

Figure 4.9 shows the distribution of 36 GHz masers that we observed in S255 (taken from Figure 3.5) in the bottom left panel. The top panel on the left, taken from Wang et al. (2011), shows red and blue contours depicting redshifted and blueshifted outflows respectively in the region. The right panel, taken from Minier et al. (2000), shows a map of 6.7 GHz Class II masers. The four 6.7 GHz masers that line up along an approximately northeast-southwest line in the right panel may be aligned along an accretion disk. Again, our observed 36 GHz masers are consistent with alignment along a line perpendicular to this direction (as seen in the bottom panel), but note that two masers cannot constrain such an alignment uniquely.

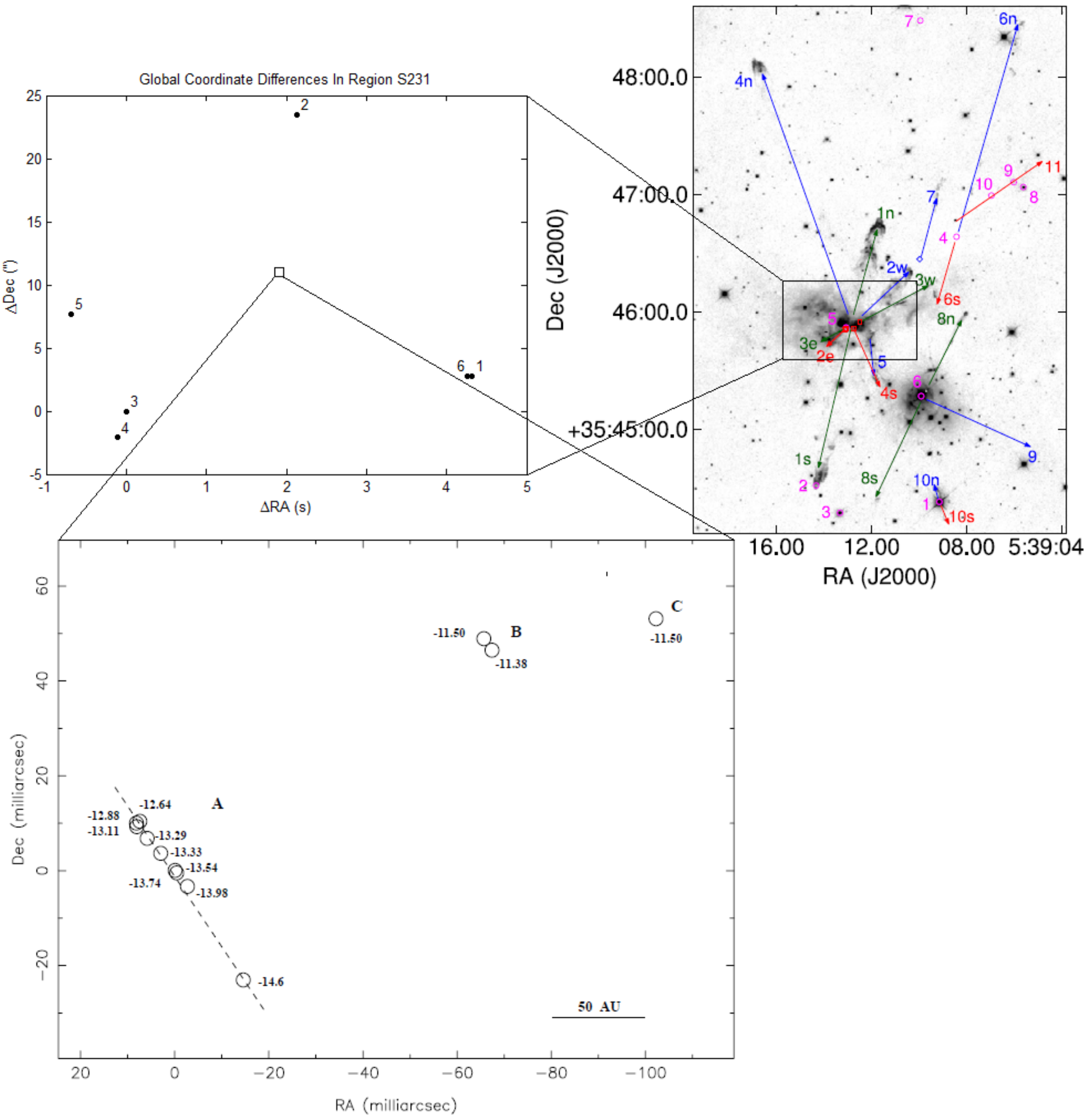

FIGURE 4.8: Plot showing the distribution of 36 GHz masers in S231 in reference to other known features. The distribution of 36 GHz masers from the observations reported in this thesis is shown in the top left panel (taken from Figure 3.1). The top right panel shows a map of H_2 emission taken from Ginsburg et al. (2009); proposed outflows are marked with arrows. The bottom panel shows a map of 6.7 GHz masers in the region (Minier et al. 2000). While absolute position information is not available for our 36 GHz masers, approximate scalings between each figure are shown by the various inset boxes.

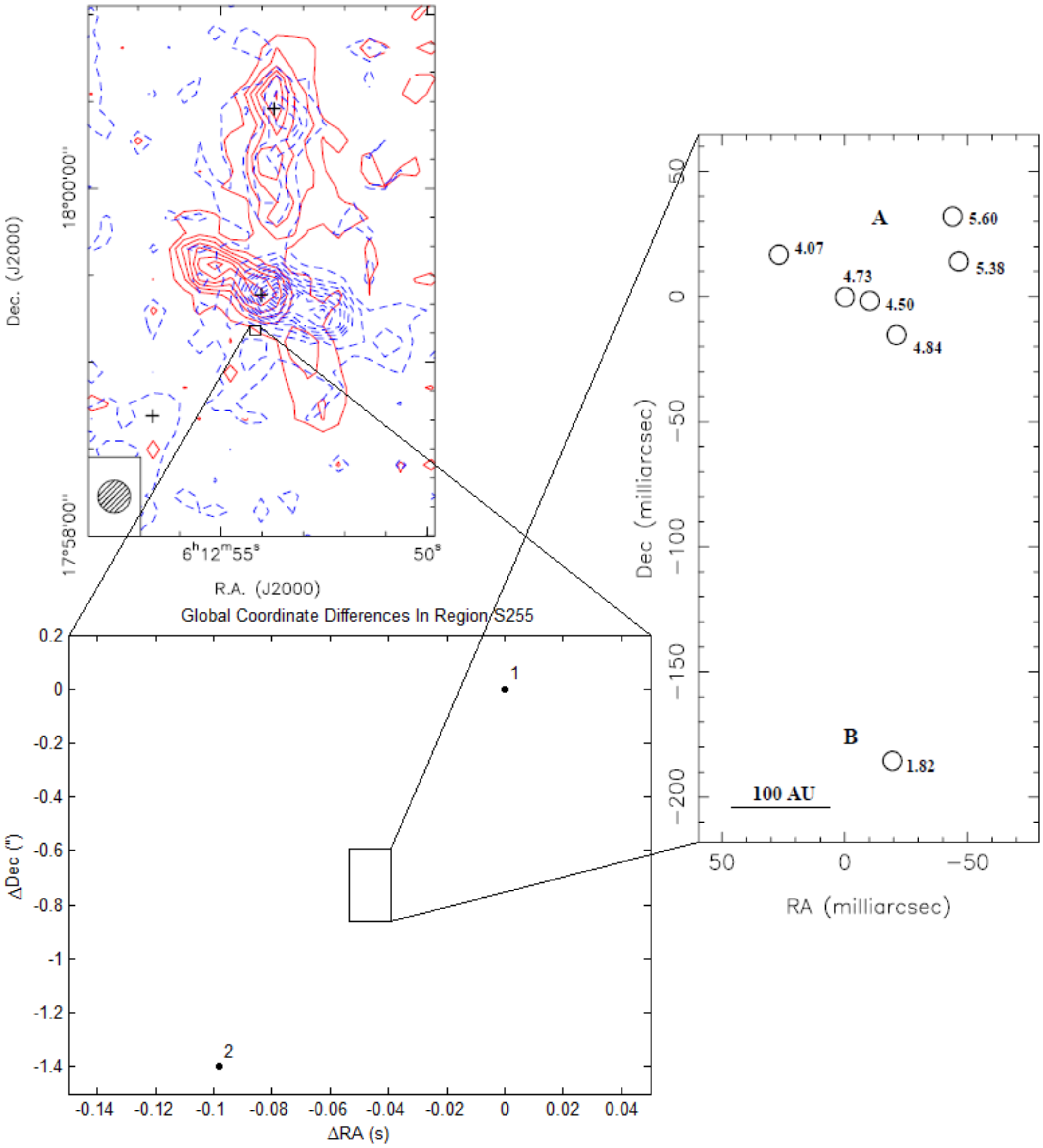

FIGURE 4.9: Plot showing the distribution of 36 GHz masers in S255 (bottom left panel, taken from Figure 3.5) in reference to other known features. The top left panel shows outflows via redshifted and blueshifted emission contours (Wang et al. 2011). The right panel shows 6.7 GHz masers from Minier et al. (2000). While absolute position information is not available for our 36 GHz masers, approximate scalings between each figure are shown by the various inset boxes.

Chapter 5

Conclusion

We detected 23 Class I methanol masers at 36 GHz in 7 star forming regions with the VLA. We plotted Gaussian profiles for all masers in order to study their distribution and line parameters.

We compared the line parameters of our observed 36 GHz masers to 6.7 GHz Class II methanol masers obtained from the literature. We found that strong 6.7 GHz masers appear to be generally associated with weak 36 GHz Class I masers. Such an anti-correlation is consistent with a similar anti-correlation between 44 GHz Class I and 6.7 GHz Class II masers, but differs from a correlation found between 95 GHz Class I and 6.7 GHz Class II methanol masers. This points to the need for a larger sample of 6.7 GHz and 36 GHz masers at high angular resolution, and the need for theoretical models of maser pumping and propagation. With both 36 GHz and 6.7 GHz receivers now available on the VLA, such high angular resolution observations are finally possible.

We also compared the center velocities ($v_{\rm LSR}$) of our observed 36 GHz masers with those of 6.7 GHz masers taken from the literature. These center velocities appear to be comparable to within about 7 km s^{-1} for the same star forming region, and are much smaller than the spread in the $v_{\rm LSR}$ of H_2O masers in such regions. The center velocities of the 6.7 GHz masers are different from the systemic velocities of these regions, likely because they are participating in rotation and expansion of the disk material in which they are excited by radiative processes. Some of the 36 GHz maser velocities appear to be quite close to the systemic velocity, and we speculate that this may be due to random chance, or because these masers are at the base of the outflow; the current observations do not have enough masers to distinguish between these scenarios.

By looking at profile differences, we conclude that stronger 36 GHz masers are likely closer to the 6.7 GHz masers, and therefore closer to the inner parts of the outflow where the shocks would be stronger. Also, the two classes of masers may be excited in different epochs.

In summary, our pilot project reveals exciting possibilities for the future of this young field. Already, our pilot observations have provided the first high angular resolution maps of 36 GHz masers in seven star forming regions. In a number of cases, our observations have also revealed alignments along larger scale outflows detected in other tracers. In at least two regions, our observations appear to suggest a disk-outflow picture when viewed in conjunction with 6.7 GHz maser observations taken from the literature.

Appendix A

Velocity Profiles with Fits

Here we present the velocity profiles of each 36 GHz methanol maser, separated by region. Data points are plotted as stars and the Gaussian fit is a solid line. Note that the horizontal and vertical axis scales are different for each figure.

A.1 S231

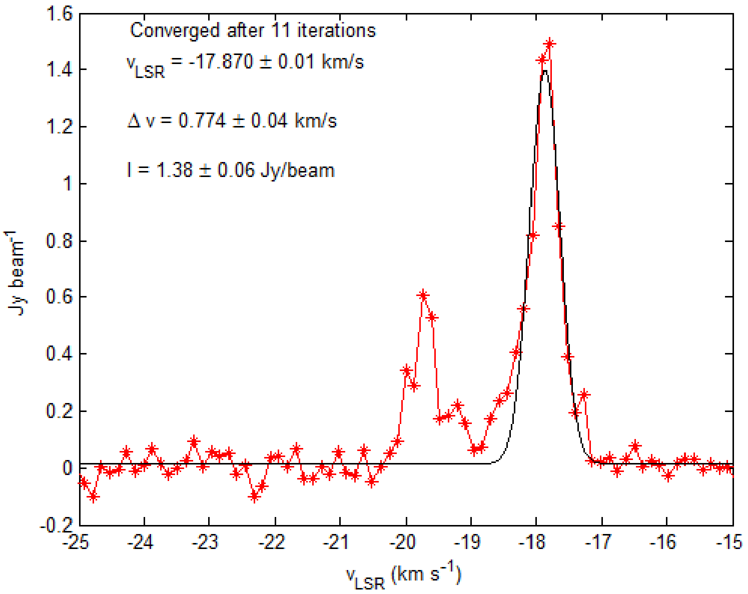

FIGURE A.1: Velocity profile and Gaussian fit of object 1 in region S231.

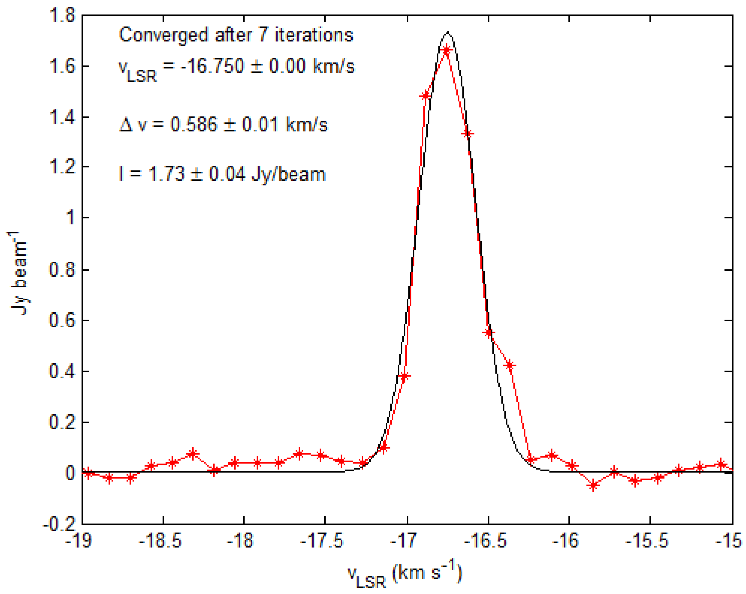

Figure A.2: Velocity profile and Gaussian fit of object 2 in region S231.

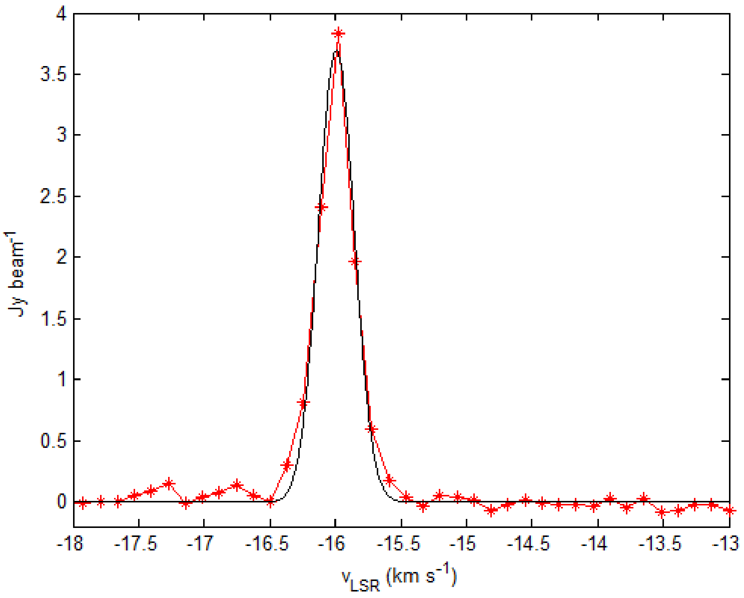

Figure A.3: Velocity profile and Gaussian fit of object 3 in region S231.

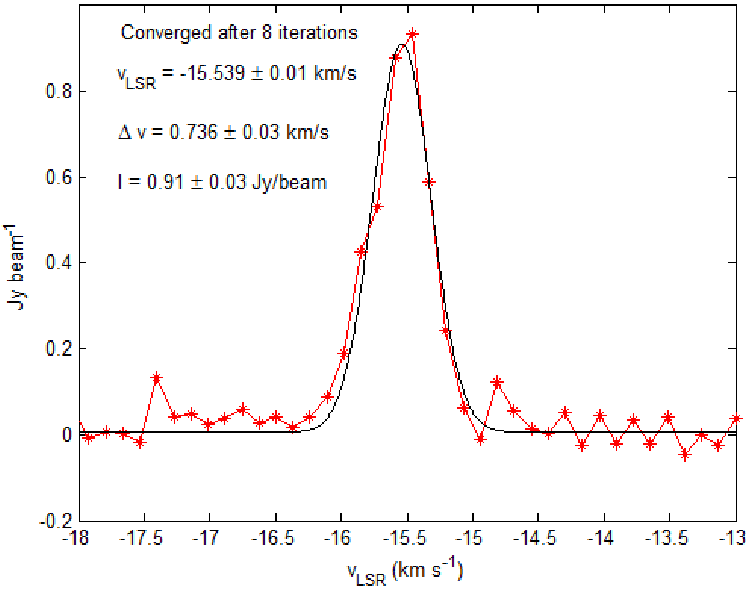

Figure A.4: Velocity profile and Gaussian fit of object 4 in region S231.

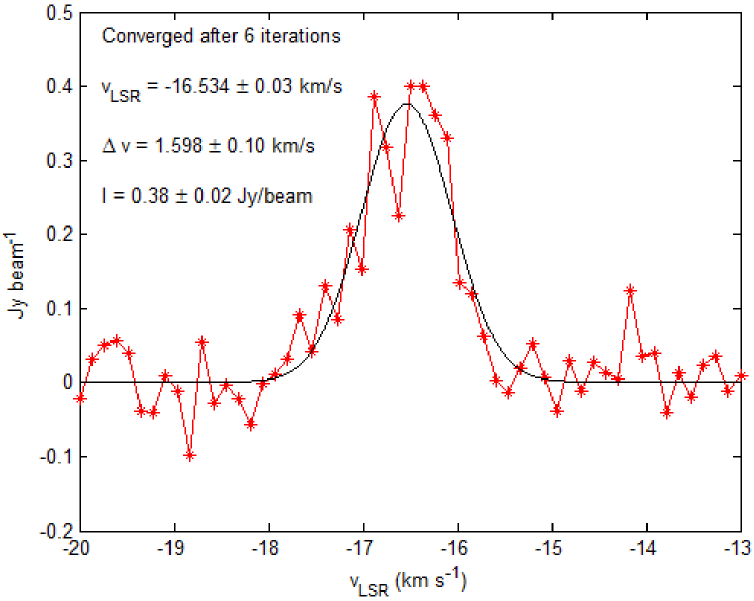

Figure A.5: Velocity profile and Gaussian fit of object 5 in region S231.

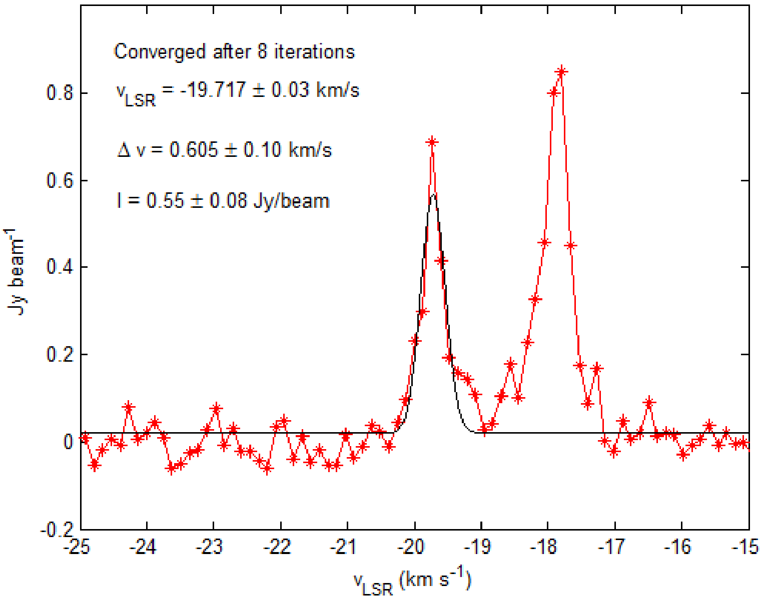

Figure A.6: Velocity profile and Gaussian fit of object 6 in region S231.

A.2 W75N

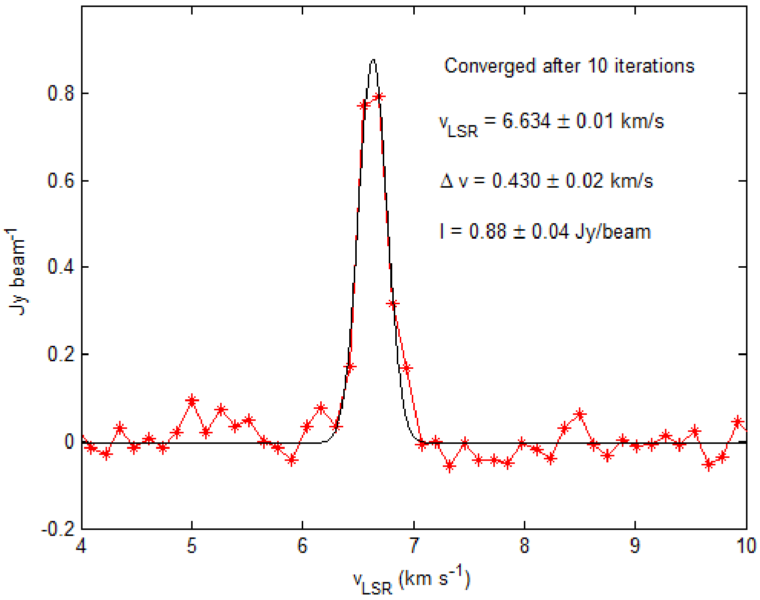

FIGURE A.7: Velocity profile and Gaussian fit of object 1 in region W75N.

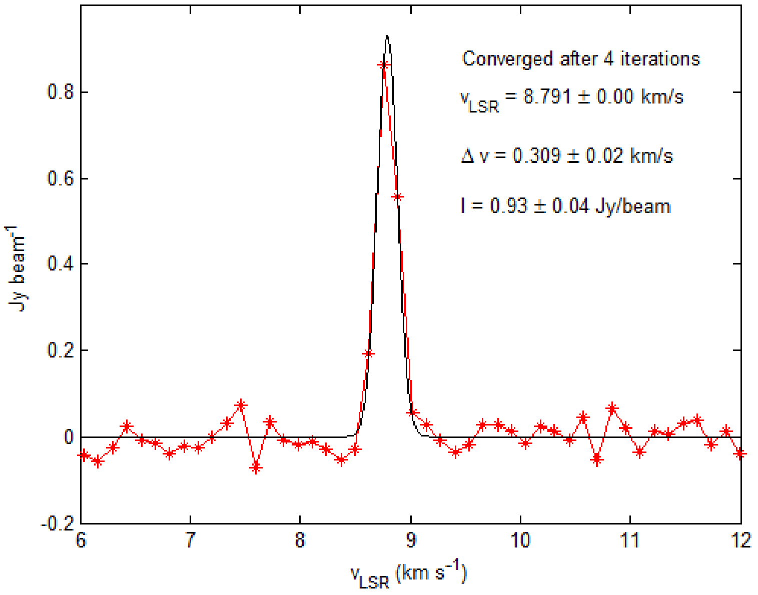

FIGURE A.8: Velocity profile and Gaussian fit of object 2 in region W75N.

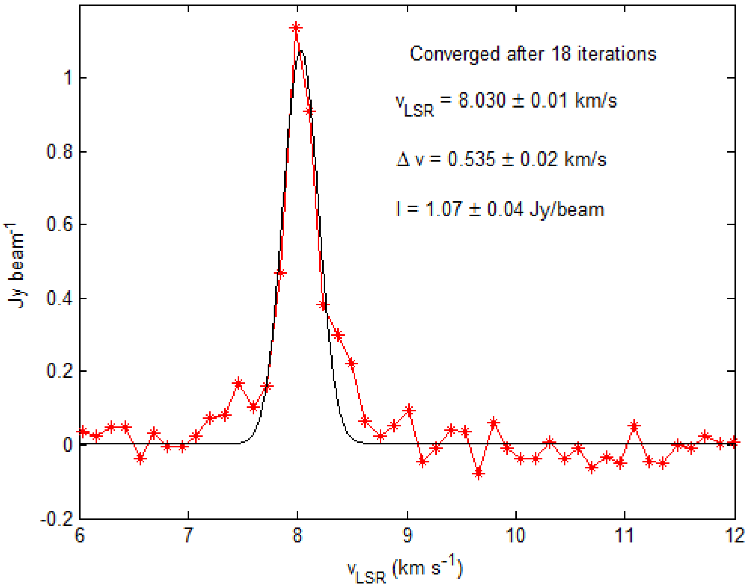

FIGURE A.9: Velocity profile and Gaussian fit of object 3 in region W75N.

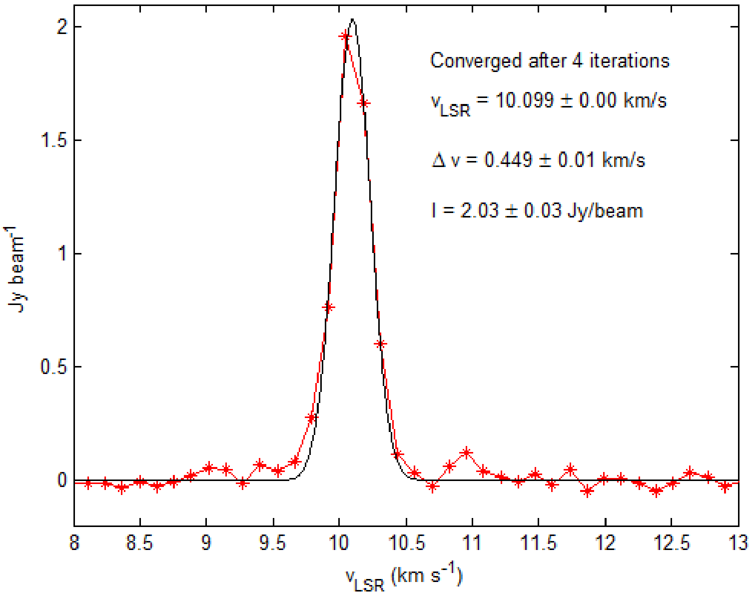

FIGURE A.10: Velocity profile and Gaussian fit of object 4 in region W75N.

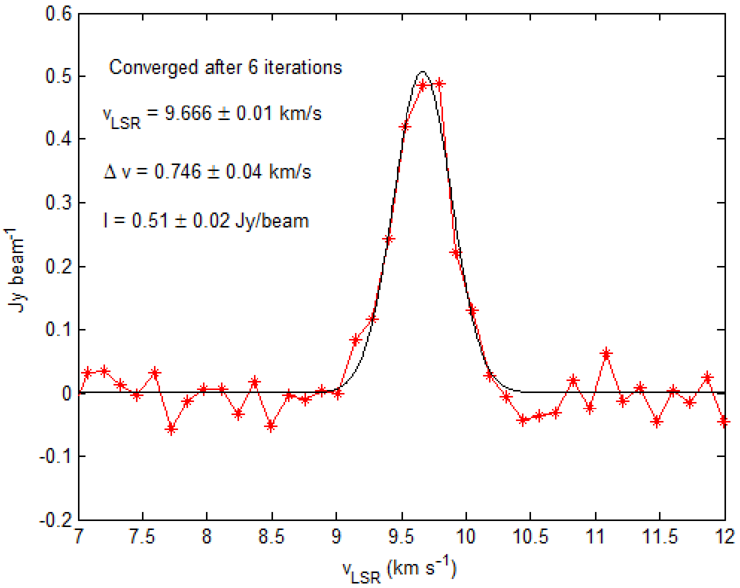

FIGURE A.11: Velocity profile and Gaussian fit of object 5 in region W75N.

A.3 W41

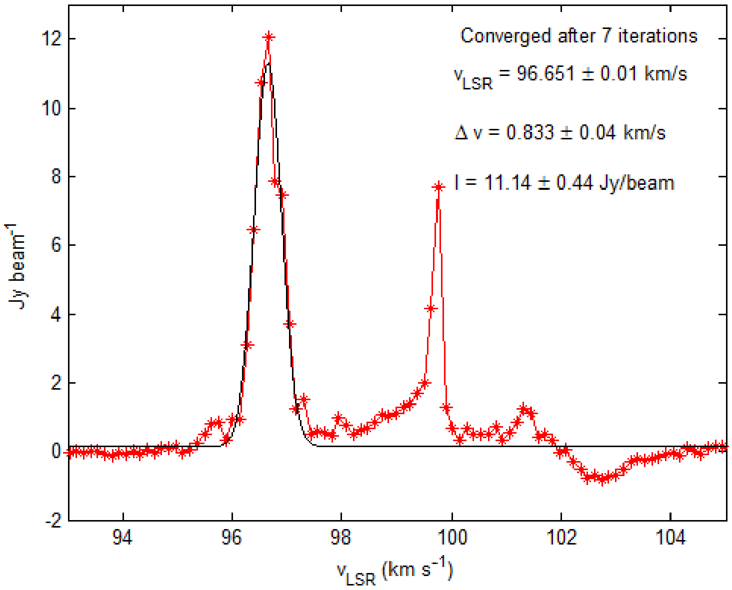

FIGURE A.12: Velocity profile and Gaussian fit of object 1 in region W41.

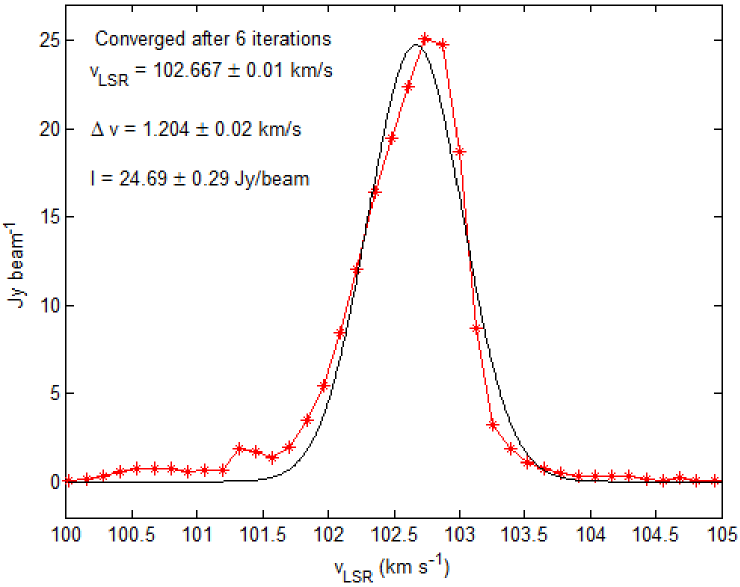

FIGURE A.13: Velocity profile and Gaussian fit of object 2 in region W41.

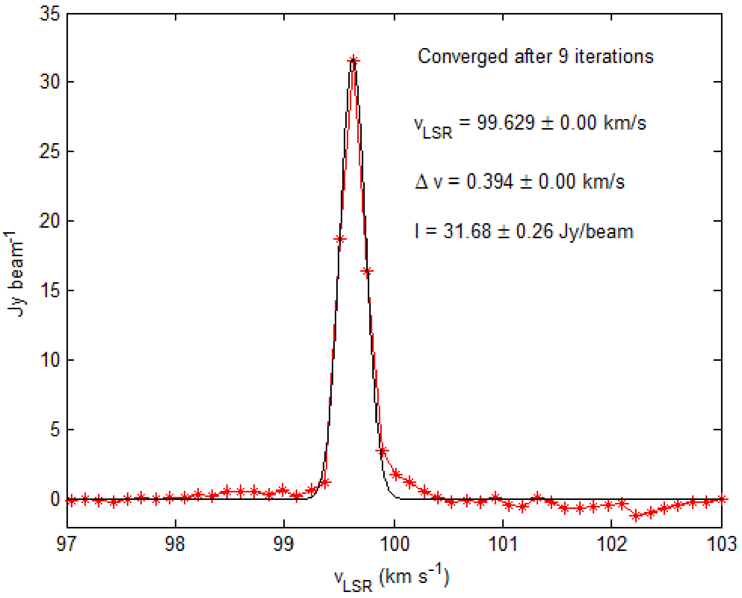

FIGURE A.14: Velocity profile and Gaussian fit of object 3 in region W41.

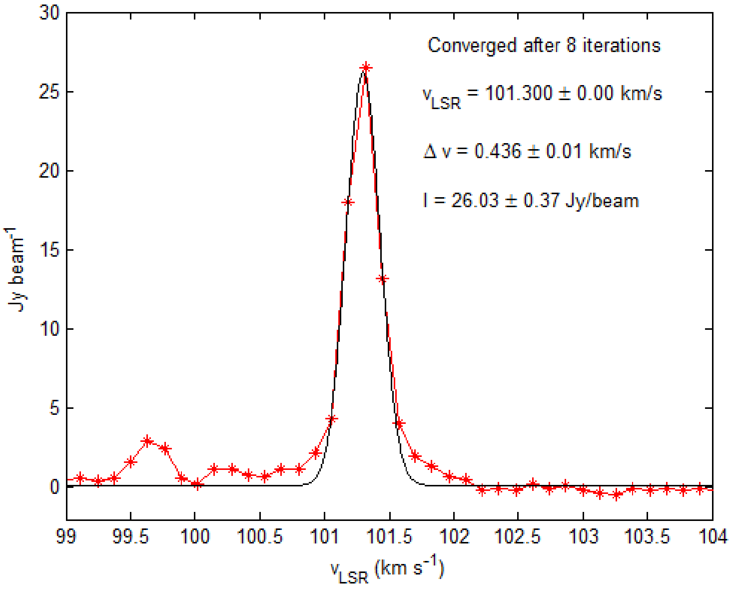

FIGURE A.15: Velocity profile and Gaussian fit of object 4 in region W41.

A.4 W42

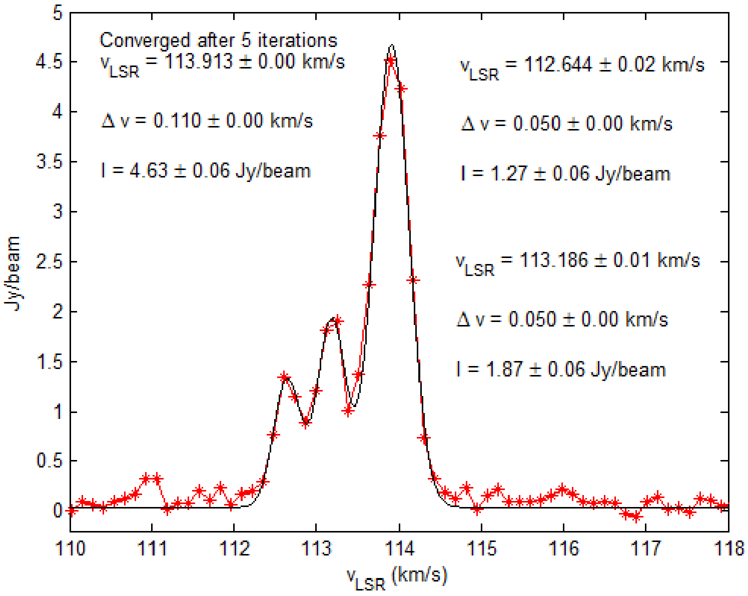

FIGURE A.16: Velocity profile and Gaussian fit of object 1 in region W42.

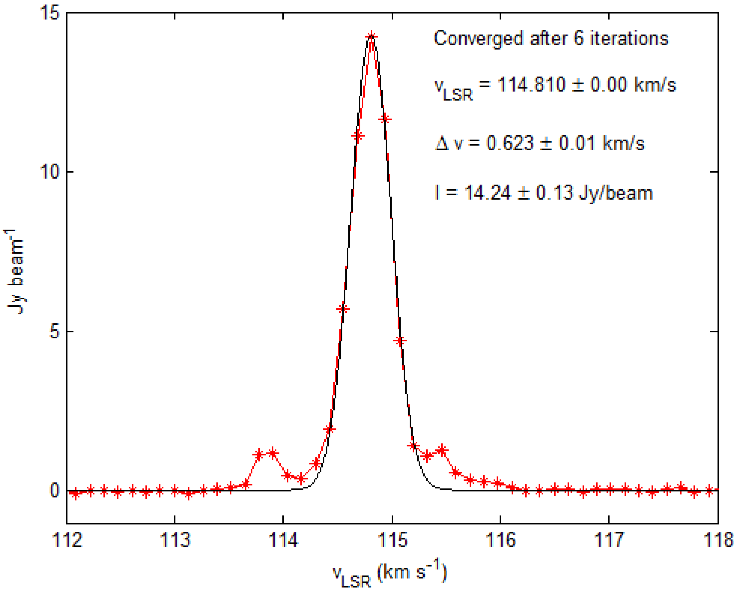

FIGURE A.17: Velocity profile and Gaussian fit of object 2 in region W42.

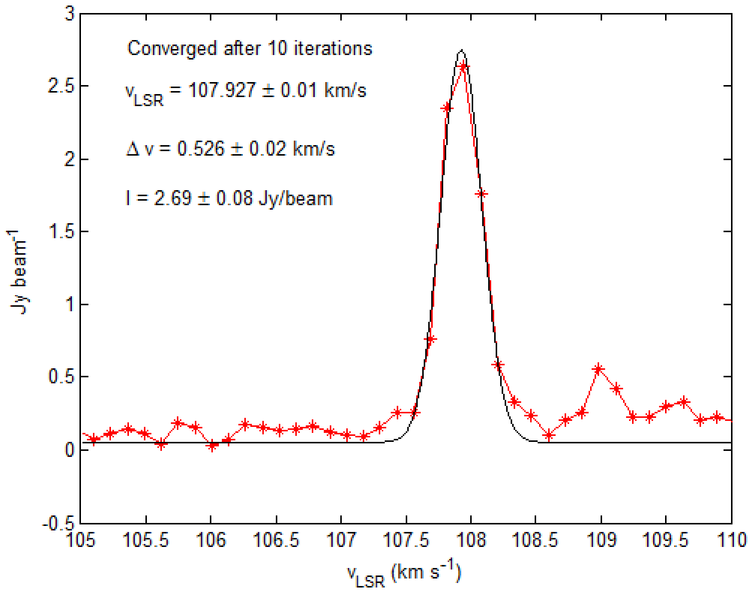

FIGURE A.18: Velocity profile and Gaussian fit of object 3 in region W42.

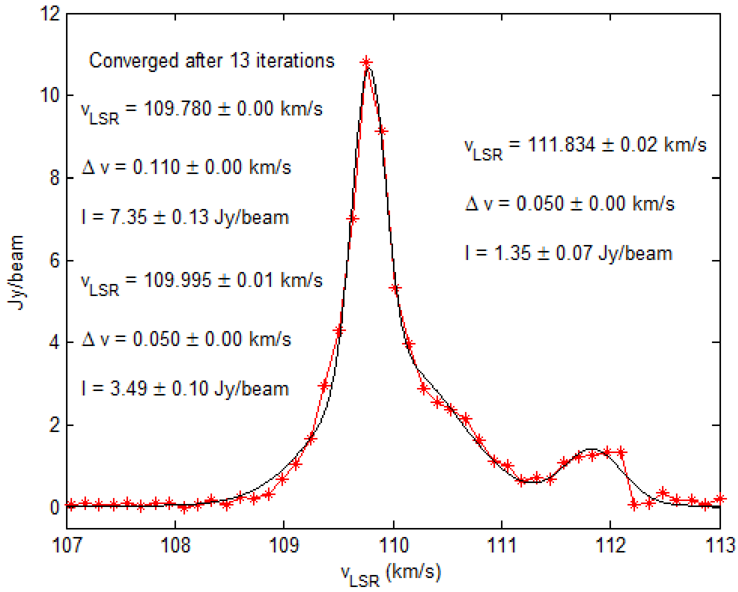

FIGURE A.19: Velocity profile and Gaussian fit of object 4 in region W42.

A.5 S255

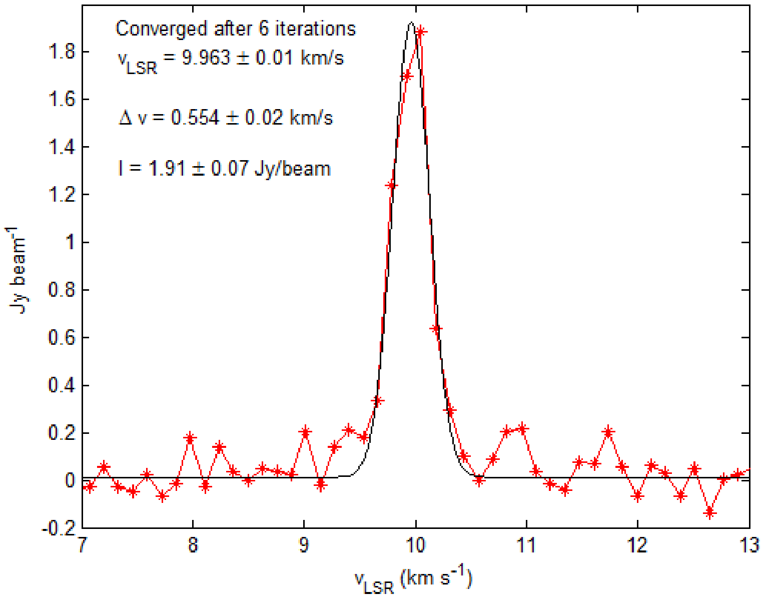

Figure A.20: Velocity profile and Gaussian fit of object 1 in region S255.

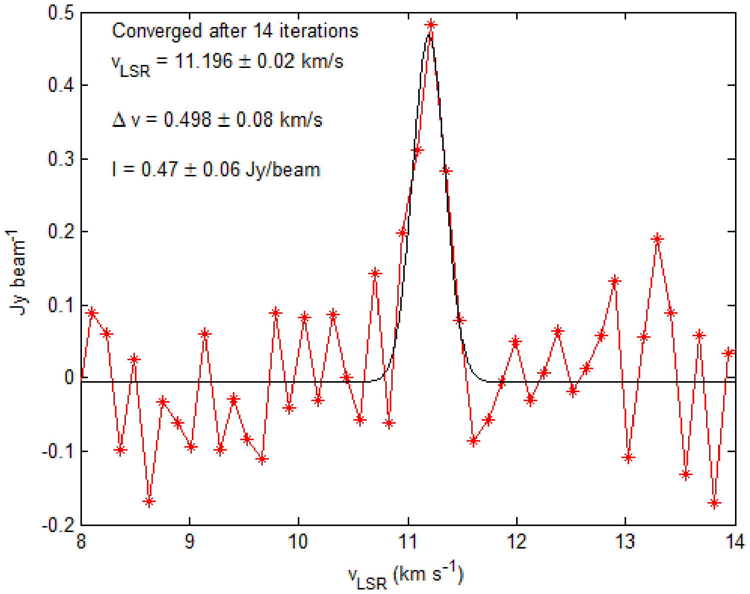

Figure A.21: Velocity profile and Gaussian fit of object 2 in region S255.

A.6 23.01-0.4

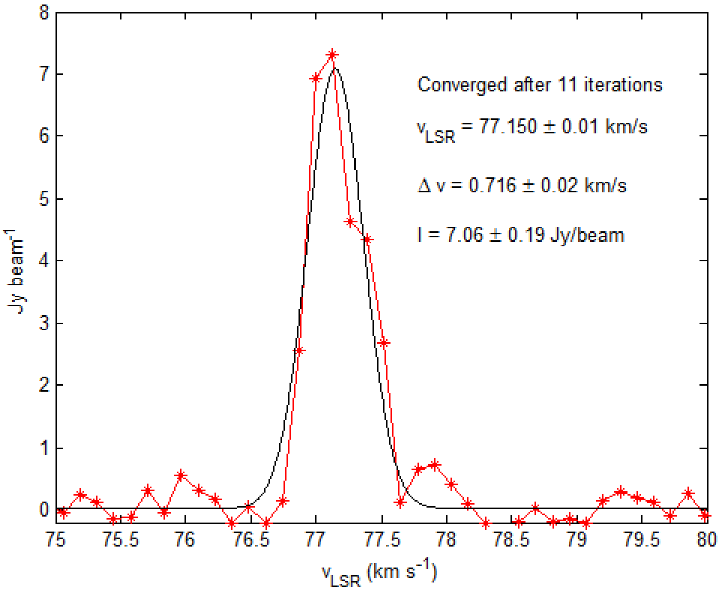

FIGURE A.22: Velocity profile and Gaussian fit of object 1 in region 23.01-0.4.

A.7 29.86-0.04

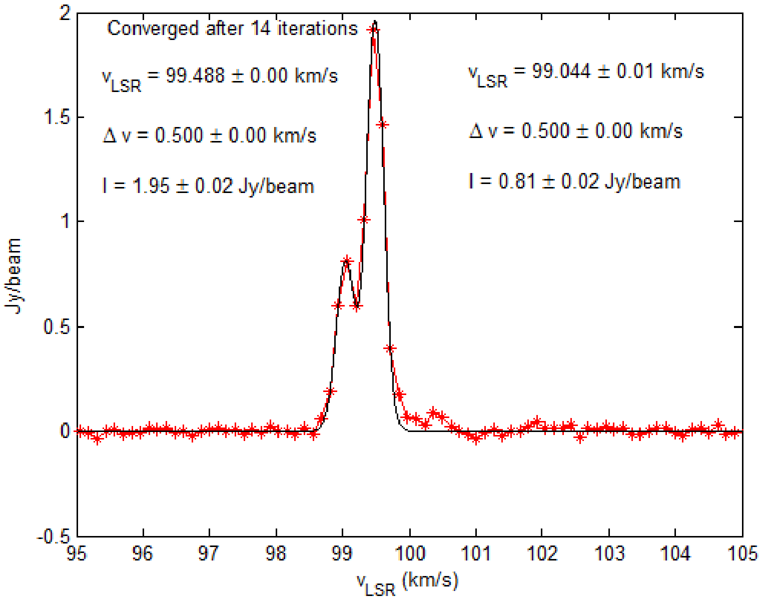

FIGURE A.23: Velocity profile and Gaussian fit of object 1 in region 29.86-0.04.

Appendix B

Data Tables

Table B.1: Data for Associated 6.7 GHz Masers. References a and b refer to Caswell et al. (2000) and Minier et al. (2000), respectively.

Region	Intensity (Jy)	Center Velocity v_{LSR} (km s^{-1})	Velocity Width (km s^{-1})	Reference
S231	208	-12.8	1.5	b
W75N	1080	7.12	0.4	b
W41	42.1	103.2	16	a
W42	82	108.6	8	a
S255	72	4.62	0.4	a
23.01-0.4	405	74.8	3	a
29.86-0.04	67	101.4	1	a

Table B.2: Systemic Velocities for Observed Regions. Reference a, b, c, d, e, f refer to Furuya (2008), Kim and Koo (2001), Brand and Blitz (1993), Leahy and Tian (2008), Caswell and Green (2011), Haschick et al. (1981), respectively.

Region	v_{LSR} km s^{-1}	Reference
S231	-16.7	c
W75N	9.4	f
W41	111	d
W42	113	e
S255	7.5	c
23.01-0.4	77.3	a
29.86-0.04	99	b

Bibliography

J. Brand and L. Blitz. The velocity field of the out galaxy. *Astronomy and Astrophysics*, 275:67–90, 1993. URL http://adsabs.harvard.edu/abs/1993A%26A...275...67B.

J. L. Caswell and J. A. Green. Blueshifted outflow from 24.329+0.145. *Mon. Not. R. Astron. Soc.*, 411:2059–2066, 2011. URL http://adsabs.harvard.edu/abs/2011MNRAS.411.2059C.

J. L. Caswell, J. Yi, R. S. Booth, and D. M. Cragg. Methanol masers at 107.0 and 156.6 ghz. *Mon. Not. R. Astron. Soc.*, 313:599–616, 2000. URL http://adsabs.harvard.edu/abs/2000MNRAS.313..599C.

D. M. Cragg, A. M. Sobolev, and P. D. Godfrey. Models of class ii methanol masers based on improved molecular data. *Mon. Not. R. Astron. Soc.*, 360:533–545, February 2005. URL http://arxiv.org/abs/astro-ph/0504194v1.

S. P. Ellingsen, D. M. Cragg, J. E. J. Lovell, A. M. Sobolev, P. D. Ramsdale, and P. D. Godfrey. Discovery of new 19.9-ghz methanol masers in star forming regions. *Monthly Notice of the Royal Astronomical Society*, 354:401–413, 2004. URL http://arxiv.org/abs/astro-ph/0407246v1.

R. S. Furuya. Condidate rotating toroids around high-mass (proto)stars. *The Astrophysical Journal*, 673:363–381, 2008. URL http://iopscience.iop.org/0004-637X/673/1/363.

A. G. Ginsburg, J. Bally, C.-H. Yan, and J. P. Williams. Outflows and massive stars in the protocluster iras 05358+3543. *The Astrophysical Journal*, 707:310–327, 2009. URL http://adsabs.harvard.edu/cgi-bin/bib_query?arXiv:0910.2990.

A. D. Haschick, M. J. Reid, B. F. Burke, J. M. Moran, and G. Miller. Vlbi aperture synthesis observations of the oh maser source w75 n. *The Astrophysical Journal*, 244:76–87, February 1981. URL http://adsabs.harvard.edu/abs/1981ApJ...244...76H.

K.-T. Kim and B.-C. Koo. Radio continuum and recombination line study of ultracompact h ii regions with extended envelopes. *The Astrophysical Journal*, 549:979–996, 2001. URL http://adsabs.harvard.edu/abs/2001ApJ...549..979K.

LAMBDA. Leiden atomic and molecular database. August 2010. URL http://home.strw.leidenuniv.nl/~moldata/CH3OH.html.

D. A. Leahy and W. W. Tian. The distances of snr w41 and overlapping h ii regions. *The Astronomical Journal*, 135:167–172, 2008. URL http://adsabs.harvard.edu/cgi-bin/bib_query?arXiv:0708.3377.

S. Leurini, P. Schilke, K. M. Menten, D. R. Flower, J. T. Pottage, and L.-H. Xu. Methanol as a diagnostic tool of interstellar clouds. i. model calculations and application to molecular clouds. *Astronomy and Astrophysics*, 422:573–585, 2004. URL http://adsabs.harvard.edu/abs/2004A&A...422..573L.

V. Minier, R. S. Booth, and J. E. Conway. Vlbi observations of 6.7 and 12.2 ghz methanol masers towards high mass star-forming regions i. observational results: protostellar disks or outflows? *Astronomy and Astrophysics*, 362:1093–1108, 2000. URL http://adsabs.harvard.edu/abs/2000A%26A...362.1093M.

R. Perley. Fundamentals of radio astronomy. May 2012. URL http://www.aoc.nrao.edu/events/synthesis/2012/lectures.shtml.

P. Pratap, P. A. Shute, T. C. Keane, and Cara. Class i methanol masers: Signposts of star formation? *The Astronomical Journal*, 135:1718–1730, May 2008. URL http://dx.doi.org/10.1088/0004-6256/135/5/1718.

D. S. Shepherd, L. Testi, and D. P. Stark. Clustered star formation in w75n. *The Astrophysical Journal*, 584:882–894, February 2003. URL http://iopscience.iop.org/0004-637X/584/2/882/fulltext/56873.text.html.

V.I. Slysh, S.V. Kalenskii, I.E. Val'tts, and R. Otrupcek. The parkes survey of methanol masers at 44.07 ghz. *Mon. Not. R. Astron. Soc.*, 268:464–474, 1994. URL http://adsabs.harvard.edu/abs/1994MNRAS.268..464S.

G. Surcis, W. H. T. Vlemmings, R. Dodson, and H. J. van Langevelde. Methanol masers probing the ordered magnetic field of w75n. *Astronomy and Astrophysics (accepted)*, 506:757, 2009. URL http://arxiv.org/abs/0908.3585.

Orazio Svelto. Principles of laser physics, 2009.

J. M. Torrelles, J. F. Gómez, N. A. Patel, S. Curiel, G. Anglada, and R. Estalella. Vlbi multi-epoch water maser observations toward massive protostars. *IAU*, 287, 2012. URL http://arxiv.org/abs/1204.3811v1.

Y. Wang, H. Beuther, A. Bik, T. Vasyunina, Z. Jiang, E. Puga, H. Linz, J. A. Rodón, Th. Henning, and M. Tamura. Different evolutionary stages in the massive star-forming region s255 complex. *Astronomy and Astrophysics*, 527:A32, 2011. URL `http://dx.doi.org/10.1051/0004-6361/201015543`.